

Dissertations and Theses

12-2015

Design, Fabrication, and Testing of a Proprioceptive Electroadhesion Pad for Space Applications

Walter Saravia

Follow this and additional works at: <https://commons.erau.edu/edt>



Part of the Aerospace Engineering Commons

Scholarly Commons Citation

Saravia, Walter, "Design, Fabrication, and Testing of a Proprioceptive Electroadhesion Pad for Space Applications" (2015). *Dissertations and Theses*. 244.

<https://commons.erau.edu/edt/244>

This Thesis - Open Access is brought to you for free and open access by Scholarly Commons. It has been accepted for inclusion in Dissertations and Theses by an authorized administrator of Scholarly Commons. For more information, please contact commons@erau.edu.

DESIGN, FABRICATION, AND TESTING OF A PROPRIOCEPTIVE
ELECTROADHESION PAD FOR SPACE APPLICATIONS

A Thesis
Submitted to the Faculty
of
Embry-Riddle Aeronautical University
by
Walter Saravia

In Partial Fulfillment of the
Requirements for the Degree
of
Master of Science in Aerospace Engineering

December 2015
Embry-Riddle Aeronautical University
Daytona Beach, Florida

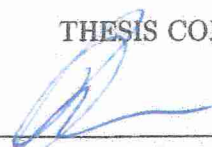
DESIGN, FABRICATION, AND TESTING OF A PROPRIOCEPTIVE
ELECTROADHESION PAD FOR SPACE APPLICATIONS

by

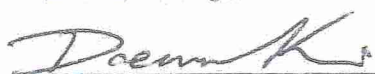
Walter Saravia

A Thesis prepared under the direction of the candidate's committee chairman, Dr. Bogdan Udrea, Department of Aerospace Engineering, and has been approved by the members of the thesis committee. It was submitted to the School of Graduate Studies and Research and was accepted in partial fulfillment of the requirements for the degree of Master of Science in Aerospace Engineering.

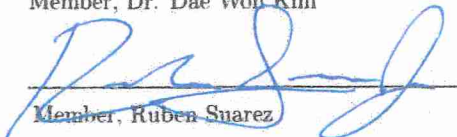
THESIS COMMITTEE



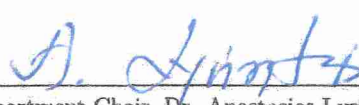
Chairman, Dr. Bogdan Udrea



Member, Dr. Dae Won Kim



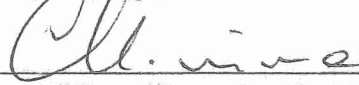
Member, Ruben Suarez



Department Chair, Dr. Anastasios Lyrintzis
or Graduate Program Coordinator, Dr. Eric Perrell

11/23/15

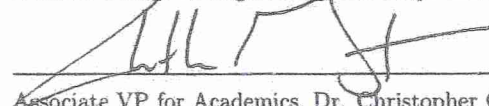
Date



Dean of College of Engineering, Dr. Maj Mirmirani

12/2/15

Date



Associate VP for Academics, Dr. Christopher Grant

11/24/15

Date

ACKNOWLEDGMENTS

I wish to express my deepest gratitude to the Thesis Chairman, Dr. Bogdan Udrea, for all the invaluable mentoring and assistance over the past couple years that was crucial for the completion of this thesis.

I would like to also thank my committee members, Dr. Dae Won Kim and Ruben Reyes for their assistance and share of knowledge that was invaluable to this research. Appreciation is also due to Mike Potash and Azizzi Boutros for the use of testing equipment and assistance in experimentation of the mechanism. I would like to thank all my friends, family, and co-workers for the support and encouragement.

Last, but not least, I would like to thank my parents and brother for all the help and support received throughout my studies. They are always pushing me to follow my dreams and never give up.

TABLE OF CONTENTS

	Page
LIST OF TABLES	vi
LIST OF FIGURES	vii
SYMBOLS	xi
ABBREVIATIONS	xii
ABSTRACT	xiii
1 Introduction	1
1.1 Electrostatic Adhesion	1
1.1.1 History of Electroadhesion	1
1.1.2 Current State of the Art in Electroadhesion Devices	5
1.1.3 Use of Electroadhesion Mechanisms for Space Applications	6
1.2 Macro Fiber Composites for Electrostatic Device Actuation	9
1.2.1 History of MFCs	10
1.2.2 Composition of MFCs	10
1.3 Research Motivation	14
2 Theoretical Background	15
2.1 Flat Plate Capacitor Models	15
2.1.1 Coulomb's Law (Direct Method)	17
2.1.2 Energy Conservation Law (Indirect Method)	18
2.2 Electric Field in Electroadhesion Applications	20
2.3 MFC calculations	24
2.3.1 Theoretical Calculations	25
3 Design of Electroadhesion Pad	27
3.1 Design Requirements	27
3.2 Finalized Designs	31
4 Finite Element Analysis	34
4.1 Purpose	35
4.2 Methodologies	38
4.2.1 Pre-processing	38
4.2.2 Processing	40
4.2.3 Post-processing	40
4.3 Assumptions	41

	Page
4.4 FEA Results	42
4.4.1 Effect of Electrode Gap on the Electric Field	42
4.4.2 Effect of Substrate Thickness on the Electric Field	45
4.4.3 Spiral Electrode Pad Analysis	49
4.4.4 Four Tooth Pad Analysis	53
4.4.5 Eight Tooth Pad Analysis	55
4.4.6 Summary of Finite Element Analysis Results	59
5 Fabrication of Electroadhesion Pads	62
5.1 Initial Fabrication Method	62
5.2 Fabrication Using Etching	63
6 Experimental Verification	69
6.1 Test Purpose	69
6.2 Experimental Design	70
6.2.1 Materials and Equipment Used	70
6.2.2 Test Setup	74
6.3 Results	78
6.3.1 Electroadhesion Results	78
6.3.2 Results of Electroadhesion Using MFC	84
6.4 Comparison with Theoretical Results	86
7 Conclusions and Future Work	88
7.1 Conclusion	88
7.2 Future Work	89
REFERENCES	91
A Mesh Densities for FEA Models	94
B Electroadhesion Pad Adhesion on Curve with MFC	99
C High Voltage Testing Safety Guidelines	102
D Ferric Chloride Etching Safety Guidelines	106

LIST OF TABLES

Table	Page
1.1 Comparison between multiple gripping methods	4
4.1 Environment Within Various Physics Domains Relating to Hooke's Law	34
4.2 Dielectric Properties of Materials Used for FEA	39
4.3 FEA Results Comparison Between the 3 Main Pad Designs	60
6.1 Standard Deviation Values for Test Results	83
6.2 FEA and Experimental Results Between the 3 Main Pad Designs . . .	87
A.1 Comparison between multiple gripping methods	94

LIST OF FIGURES

Figure	Page
1.1 Typical Materials with increasing Electrical Conductivity (The Physics Classroom, 2015)	2
1.2 Objects in Earth Orbit with Respect to Time (Liou, 2010)	7
1.3 Mission Schematic for Orbital Debris Removal	8
1.4 Composition of a Macro Fiber Composite (Smart-Material, 2015)	11
1.5 Actuation direction for d31 and d33 mode (Tolliver, Xu, & Jiang, 2013)	11
1.6 d33 configuration for MFC (Smart-Material, 2015)	12
1.7 d31 configuration for MFC (Smart-Material, 2015)	12
1.8 M-8514 MFC	13
2.1 Electric field flux for parallel plate capacitor (Busse, 2004)	15
2.2 Simulation of electric field flux for parallel plate capacitor	16
2.3 Formation of Opposite Charges on Conductive Surface (Germann, 2014)	21
2.4 Polarization Between Electrodes on an Insulator Surface (Germann, 2014)	21
2.5 Dielectric Breakdown of a Spiral Pad Design	24
3.1 Example of pad designs created by other researchers (Ruffatto, 2013) .	28
3.2 Schematic of Non-actuated Electroadhesion Pad	30
3.3 Schematic of Actuated Electroadhesion Pad	30
3.4 Dimensions of Spiral Pad Design	32
3.5 Dimensions of Four Tooth Pad Design	32
3.6 Dimensions of Eight Tooth Pad Design	33
4.1 Four Tooth Large Gap Model (1 cm gap)	43
4.2 Four Tooth Small Gap Model (0.5 cm gap)	43
4.3 Four Tooth Large Gap Voltage Distribution	44
4.4 Four Tooth Small Gap Voltage Distribution	44

Figure	Page
4.5 Four Tooth Large Gap Electric Field Between Electrodes	45
4.6 Four Tooth Small Gap Electric Field Between Electrodes	46
4.7 Isometric view of Spiral Design	47
4.8 Voltage Distribution for Spiral Design	47
4.9 LF9120 Electric Field Between Electrodes for Spiral Design	48
4.10 LF9130 Electric Field Between Electrodes for Spiral Design	48
4.11 Voltage distribution for Conductive Surface	49
4.12 Electric Field Between Electrodes for Conductive Surface	50
4.13 Close Up of Electric Field Vectors Under Conductive Surface	51
4.14 Voltage distribution for Insulator Surface	51
4.15 Electric Field Between Electrodes for Insulator Surface	52
4.16 Close Up of Electric Field Vectors on the Insulator Surface	52
4.17 Voltage distribution for Conductive Surface	53
4.18 Electric Field Between Electrodes for Conductive Surface	54
4.19 Close Up of Electric Field Vectors Under Conductive Surface	54
4.20 Voltage distribution for Insulator Surface	55
4.21 Electric Field Between Electrodes for Insulator Surface	55
4.22 Close Up of Electric Field Vectors on the Insulator Surface	56
4.23 Voltage Distribution for Conductive Surface	56
4.24 Electric Field Between Electrodes for Conductive Surface	57
4.25 Close Up of Electric Field Vectors Under Conductive Surface	58
4.26 Voltage distribution for Insulator Surface	58
4.27 Electric Field Between Electrodes for Insulator Surface	59
4.28 Close Up of Electric Field Vectors on the Insulator Surface	59
5.1 Initial "U-Shape" Proof of Concept Pad	63
5.2 Cross Sectional Illustration of LF9130	64
5.3 Printed Designs on Pyralux sheet	65
5.4 Pyralux Pads Submerged in Ferric Chloride	66

Figure	Page
5.5 Etched Pads With Remaining Wax Layer	67
5.6 Completely Etched Pads with Exposed Electrode Designs	67
5.7 Spiral Pad with Insulation Tape	68
5.8 Spiral Pad with attached MFC actuator	68
6.1 Tested Pads in Air and Vacuum (Pelrine, 2009)	70
6.2 Glassman MJ3P5000 3kV Power Supply	71
6.3 Aluminum Surface used for Testing	72
6.4 Glass surface used for Testing	73
6.5 Shimpo FGV Series Force Gage	73
6.6 AMT2012-CE3 Amplifier	74
6.7 myDAQ DAQ System	74
6.8 Test Setup on Aluminum Surface	75
6.9 Schematic of Hardware Setup for MFC and Electroadhesion Pad	76
6.10 Schematic of Test Setup for MFC Actuation	76
6.11 Test Setup to Determine Adhesion with MFC Use	77
6.12 Peak Adhesion with Spiral Pad on Aluminum	78
6.13 Peak Adhesion with Spiral Pad on Glass	79
6.14 Peak Adhesion with Four Tooth Pad on Aluminum	80
6.15 Peak Adhesion with Four Tooth Pad on Glass	80
6.16 Peak Adhesion with Eight Tooth Pad on Aluminum	81
6.17 Peak Adhesion with Eight Tooth Pad on Glass	82
6.18 Average Adhesion of Pads on Aluminum	82
6.19 Average Adhesion of Pads on Glass	84
6.20 Peak Spiral Adhesion Without MFC Actuation	85
6.21 Peak Spiral Adhesion With MFC Actuation	85
6.22 Average Adhesion of Spiral Pad With MFC Off and MFC On	86
A.1 Mesh Density on Four Tooth - Large Gap Model	95
A.2 Mesh Density on Four Tooth - Small Gap Model	95

Figure	Page
A.3 Mesh Density on LF9120 Spiral Model	96
A.4 Mesh Density on LF9130 Spiral Model	96
A.5 Mesh Density on Spiral Model with Adhering Body	97
A.6 Mesh Density on Four Tooth Model with Adhering Body	97
A.7 Mesh Density on Eight Tooth Model with Adhering Body	98
B.1 Hollow Cylinder Used for Curvature Testing	100
B.2 Electroadhesion Pad with No Actuation	101
B.3 Electroadhesion Pad With Actuation	101

SYMBOLS

a	computational coefficients
C	capacitance
d_{33}	piezoelectric coupling effect coefficient
D_1	bending modulus per unit width
E_3	electric field in third direction
E	electric field
E_{MFC}	modulus of MFC
E_s	substrate modulus
e	element number
F_b	blocking force of MFC
F	electrostatic force
f	force density
$[k]$	stiffness matrix
L	length of MFC
l	plate distance
m	total number of elements
Q_j	free charge matrix
Q	stored charge
q	charge
$[S_{ij}]$	global stiffness matrix
S	surface area of plate
t_{MFC}	thickness of MFC
t_s	substrate thickness
U	voltage gradient
$\{u\}$	displacement vector
V_{app}	applied voltage
V	voltage
v_i	electric field potential matrix
v	electric potential
W	work (energy)
w	width of MFC
∇	divergence operator
δ	deflection
ϵ_0	free space permittivity
ϵ	permittivity
ϕ	electric flux
σ	charge density

ABBREVIATIONS

NASA	National Aeronautics and Space Administration
MFC	Macro Fiber Composite
mph	Miles Per Hour
mm	Millimeter
cm	Centimeter
m	Meter
N	Newton
FEA	Finite Element Analysis
CAD	Computer Aided Drafting
DC	Direct Current
PPE	Personal Protective Equipment
C	Celsius
mA	Milliamps
W	Watts
PC	Personal Computer

ABSTRACT

Saravia, Walter MSAE, Embry-Riddle Aeronautical University, December 2015. Design, Fabrication, and Testing of a Proprioceptive Electroadhesion Pad for Space Applications.

The purpose of this study is to design, analyze, and fabricate an electroadhesion mechanism with the goal of providing controlled electrostatic adhesion to objects with little known surface finish, of varying curvature, and different materials. The main purpose of the mechanism is that of ensuring a soft docking, controlled in closed loop, for attachment to large pieces of orbital debris. Other envisaged purposes for the mechanism are sample collection and manipulation in free-fall and in-situ analysis of cohesive forces in regolith at small bodies, such as asteroids or comets. Electrostatic finite element analysis was performed on various electroadhesion pad designs in order to compare field intensities. In order to obtain optimum surface adhesion, the use of Macro Fiber Composite (MFC) actuators were embedded on the electroadhesion pad. Fabrication methods involving the use of a chemical etching process on copper clad composites were used in order to test the pads and determine the level of adhesion obtained. The design methods, fabrication techniques, and experimental results are presented.

1. Introduction

1.1 Electrostatic Adhesion

1.1.1 History of Electroadhesion

Electrostatic attraction was known since the early days of the ancient Greeks. Greek philosopher Thales of Miletus, who lived around 600 B.C., noticed that when a piece of amber (fossilized tree sap) was rubbed, light objects such as feathers were attracted to it (Ashall, 1994). In fact, the word electricity comes from the Greek work electron, which means amber. However, no theories were obtained for this phenomena based on the Greeks observations at the time.

In the late 1700's, several experiments were performed by French scientist Charles Augustin de Coulomb in order to determine the variables that affect electrical force. Around 1785, he stated that opposite charges attract and like charges repel which became Coulomb's Law (Brain & Lamb, 2004). Based on Coulomb's law, the electrostatic forces are proportional to the products of the charges and inversely proportional to the square distance between charges. Although the electrostatic forces could be calculated at this point, it was still rather unknown as to where the charges came from.

The existence of electrons was fully discovered in 1897 by an English physicist named Joseph John Thomson (*The Oxford companion to the history of modern science*, 2003). Materials can typically be categorized as either electrical insulators, semi-conductors, or conductors. They are distinguished by how the electrons interact with the atoms within the material. Materials in which the electrons are tightly constrained with their atoms cannot conduct electricity efficiently, and are considered electrical insulators. Some examples of electrical insulators are rubbers, glass, wood, and plastics. Electrons of metal atoms can easily separate from their atoms and move freely. The free moving electrons in the metal allow electricity to flow through the materials. Metals are considered electrical conductors such as aluminum, steel, copper, and silver. Figure 1.1 shows typical materials with increasing electrical conductivity.

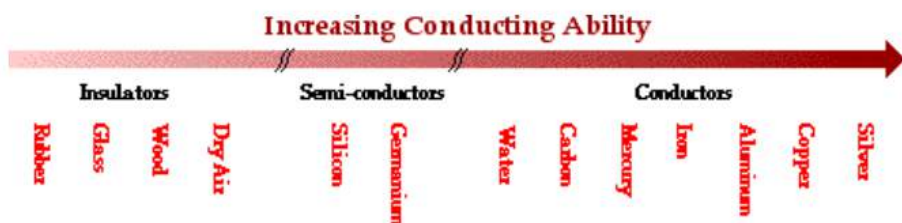


Figure 1.1. Typical Materials with increasing Electrical Conductivity
(The Physics Classroom, 2015)

Electroadhesion is essentially the effect of adhesion between two surfaces when subjected to an electric field generated by a charge differential across a dielectric. Electrostatic forces can be obtained in order to adhere to most types of materials whether they are insulators or conductors. Electroadhesive mechanisms have been

used for many years in various industries as a form of gripping or retrieval system. Around the 1960's, NASA had experimented with the use of electroadhesion to allow astronauts or robots to walk outside space vehicles when in orbit (Krape, 1968). Electroadhesion entered the industrial world in the 1980's with the use of robotics in manufacturing. The handling of sheet materials such as polymers, textiles, and carbon fiber were done by some manufacturers through the use of electroadhesion (Monkman, 2003).

There has been a great interest over the past couple years of designing a compliant, efficient, cost-effective electroadhesion pad that can adhere to a wide variety of surface types. There are other existing methods of gripping systems such as chemical adhesion, suction cups, synthetic gecko feet (Parness, 2013), magnetic, and mechanical grippers. Each method has attributes that make it desirable, but each also has unfavorable attributes for space use. Chemical adhesion, for example, can generate a strong bond, but can not be re-used once the bond has been set. The bonding agents would also have to be able to cure in space conditions in lack of oxygen. Suction cups usually create high adhesion force, but would not function in a space environment due to lack of air. Synthetic gecko feet are also an alternate gripping method currently being investigated. Using gecko feet through the Van Der Waals effect can generate strong adhesion, but has difficulty adhering to rough surfaces (SRI International, 2010). Magnetic grippers can provide strong adhesion, but their use is limited to only ferromagnetic surfaces. Since space objects are fabricated from a wide range of materials including insulators such as glass or mylar, the use of magnets would

not be suitable. Mechanical arms, such as robotic arms, are commonly used on space stations to handle large payloads. The disadvantage with mechanical arms is that they are usually pre-designed to grip certain space objects and are quite complex in dynamics and control.

Table 1.1. Comparison between multiple gripping methods

Method Type	Advantage	Disadvantage
Chemical	<ul style="list-style-type: none"> Strong Bond Can be used on multiple surface types 	<ul style="list-style-type: none"> Cannot be reused
Suction	<ul style="list-style-type: none"> High Force Low cost 	<ul style="list-style-type: none"> Poor performance on rough surfaces Will not create suction in space
Synthetic Gecko Feet	<ul style="list-style-type: none"> Non-damaging/No residue 	<ul style="list-style-type: none"> Poor performance on rough surfaces
Magnetic	<ul style="list-style-type: none"> High force capability 	<ul style="list-style-type: none"> Only works on ferromagnetic surfaces
Mechanical Gripper	<ul style="list-style-type: none"> High force capability Can usually be manipulated 	<ul style="list-style-type: none"> Usually designed for specific space bodies/applications
Electroadhesion	<ul style="list-style-type: none"> Repeated Use Works on rough and smooth surfaces Low cost Consist of space rated materials 	<ul style="list-style-type: none"> Relatively lower adhesion force Dependent on surface contact area

The main advantage of electroadhesion is that it can be repeatedly used on various rough, smooth, and on dusty surfaces. Even when dusty surfaces are present, adhesion can still be achieved. With electroadhesion pads, no residue or damage to the substrate is left behind like other methods, such as chemical adhesion. Also, due to the simplicity of the required materials to make an electroadhesion pad, the materials used are typically space rated materials (Pelrine, 2009). Electroadhesion pads are able

to adhere to various types of surfaces whether they are conductive, semi-conductive, or insulating surfaces (Koh, 2014). A drawback on electroadhesion pads is that they must be in very close contact with the adhering body in order to generate forces. Another drawback of using electroadhesion is that they produce relatively lower adhesion force than the other methods. Adhesion can be increased though, through the selection of materials and geometry. Table 1.1 shows a comparison between the advantages and disadvantages of the various gripping methods outlined.

1.1.2 Current State of the Art in Electroadhesion Devices

Electroadhesion pads typically consist of a pair of electrodes embedded within a dielectric medium. When voltage is applied, an electric field is created between the electrodes and a neighboring medium. When the electrodes are energized, electron holes are formed under the negative electrode and the negative electrons shift under the positive electrode (Germann, 2014). Essentially, the two electrodes form a capacitor when energized that result in electric charges stored within the electrodes. Opposite charges are formed on the substrate surface which causes the attraction between both bodies. There are multiple variables that control the amount of adhesion. In order to understand the variables for electrostatic forces, calculations can be performed using capacitance equations, which are discussed below in Chapter 3. The use of electroadhesion for industrial and technological purposes has been studied somewhat widely, but not much optimization has been performed in order to acquire maximum adhesion. There has been significant research conducted on the use of

electroadhesion for wall climbing robots that could be used for military or industrial applications (Liu, 2012). Military applications would consist of urban reconnaissance where robots would inspect buildings before sending in humans, which could potentially save lives. Industrial applications would consist of glass cleaning robots that perform window cleaning on large buildings. Inspection of aircraft, vessels, and power plants would also be good industrial applications that could potentially save time and money.

1.1.3 Use of Electroadhesion Mechanisms for Space Applications

As mentioned earlier, there have been studies conducted with electroadhesion for use in space applications. More recent studies have been completed in an effort to create an electroadhesion mechanism that can be used as a gripping tool. There are many uses for a reliable gripping mechanism that can be used in the harsh environment of low earth orbit. One example of space application is being able to dock with retired satellites or spent upper stages in order to refuel, repair, or inspect. There is currently no universal method of docking with satellites in order to service them (Leung, 2015).

Most satellites sent in orbit are limited in the amount of propellant they carry, hence can go out of commission once they have depleted it. Mission duration can potentially be increased if the satellite is able to be docked and refueled or repaired. Most gripping methods currently available for space applications are designed for

satellite-specific connections and are often not universal for surfaces on unknown material or shape.

Another use of electroadhesion in space applications is for the removal of space debris. Figure 1.2 shows a graph of number of objects in earth orbit with respect to time. As seen from the graph, one of the more noticeable spikes occurred in 2007 when a Chinese weather satellite was purposely destroyed as part of a Chinese anti-satellite test. This action resulted in over 2,300 pieces of trackable debris (Colorado.edu, 2010).

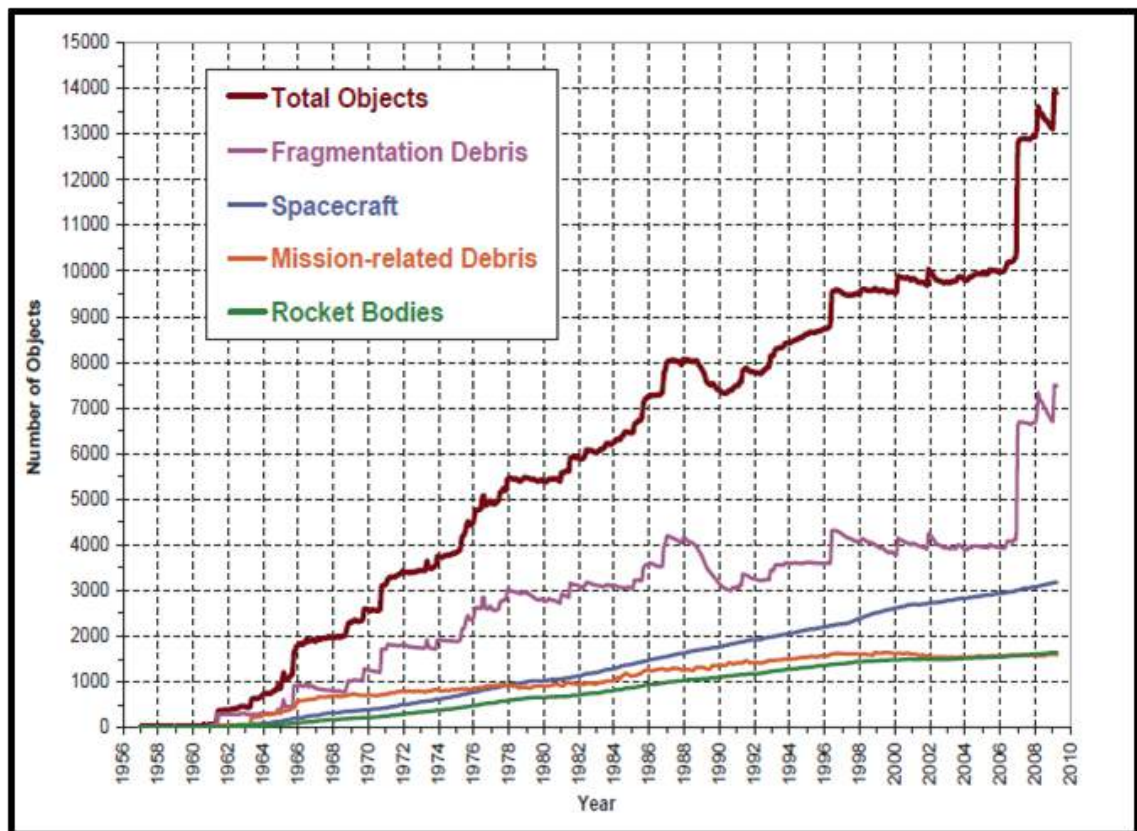


Figure 1.2. Objects in Earth Orbit with Respect to Time (Liou, 2010)

Some of the debris being tracked are traveling at speeds up to 17,500 mph (Garcia, 2013). Any object traveling at such high speeds can create catastrophic damage/failure to current spacecraft, especially if the spacecraft has humans aboard. Current plans involve having robotic debris removal systems that will use electroadhesion pads to retrieve the orbital debris. Figure 1.3 shows the overall mission schematic for the removal of an upper stage body in low earth orbit.

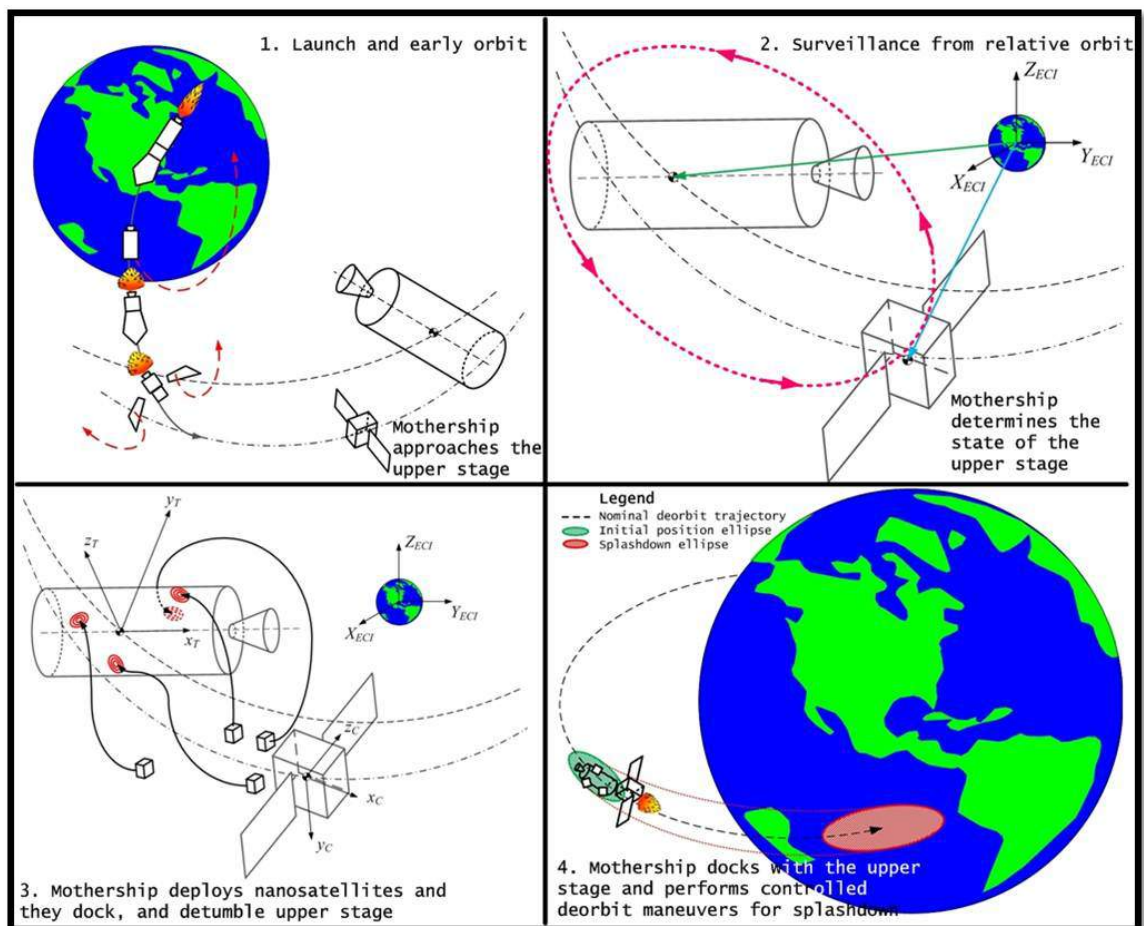


Figure 1.3. Mission Schematic for Orbital Debris Removal

First, the mothership that is to retrieve the debris is launched and approaches the upper stage body, which is debris for this example. The mothership then determines the state of the debris from a relative orbit. Within the mothership, there are nanosatellites (four in the image) that are deployed and approach the upper stage in order to dock. These nanosatellites will dock to the upper stage via electroadhesion. Due to the fact that the shape of the debris can vary, actuators are embedded within the electroadhesion device so that it conforms to curvature and results in maximum contact surface during docking. Once the upper stage body is docked with the nanosatellites and mothership, controlled deorbit maneuvers will be performed for splashdown. Since space debris can have various sizes, shapes, and materials, it is important that the docking/attachment device can conform and attach itself to a wide variety of substrates.

1.2 Macro Fiber Composites for Electrostatic Device Actuation

Although electroadhesion pads can potentially generate high adhesive forces once energized, the pads themselves need to be in close proximity to the substrate surface in order to operate efficiently. Maximum adhesion is achieved when there is maximum surface contact, with no gaps, although this is highly unlikely due to surface roughness. This also presents challenges in situations where the objects to be retrieved are of non-uniform geometry causing difficulty to allow full contact surface. For this research, the use of embedded Macro Fiber Composites (MFC) has been investigated

in order to actuate the electroadhesion pad to obtain as much surface contact as possible.

1.2.1 History of MFCs

MFCs were developed by NASA in 1996 originally for use in helicopter blades and airplane wings in order to control vibration, noise, and deflections (Turner, 2007). An MFC is a relatively low cost actuator and sensor that consists of rectangular piezo ceramic rods; which are embedded within adjacent epoxy adhesive, electrodes, and polyimide film (Smart-Material, 2015).

1.2.2 Composition of MFCs

Figure 1.4 shows the schematic structure of a typical MFC. There is a sheet of rectangular piezoceramic rods that are embedded between layers of structural epoxy, interdigitated electrodes, and polyimide film. Structural epoxy is used to bond the ceramic rods to the outer electrode layers and also to remove any potential air gaps that may cause ionization (dielectric breakdown of air). The electrodes that are attached to the polyimide film transfer the applied voltage to the ceramic rods in order for actuation to occur.

The MFCs that are commercially available have two different operational modes which are the elongation mode or the contraction mode. Figure 1.5 shows a simple representation of the actuation direction for different modes. Mode d33 allows elonga-

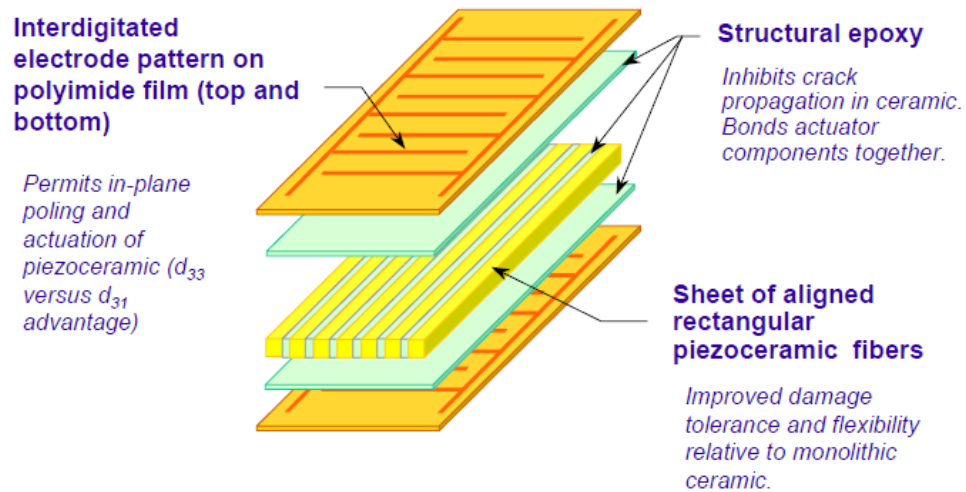


Figure 1.4. Composition of a Macro Fiber Composite (Smart-Material, 2015)

tion along the z-axis when the poling axis is parallel. This also results in contraction along the x-axis. When the poling axis is parallel to the x-axis (mode d_{31}), expansion of the solid will occur in the x-axis and contraction will occur along the z-axis.

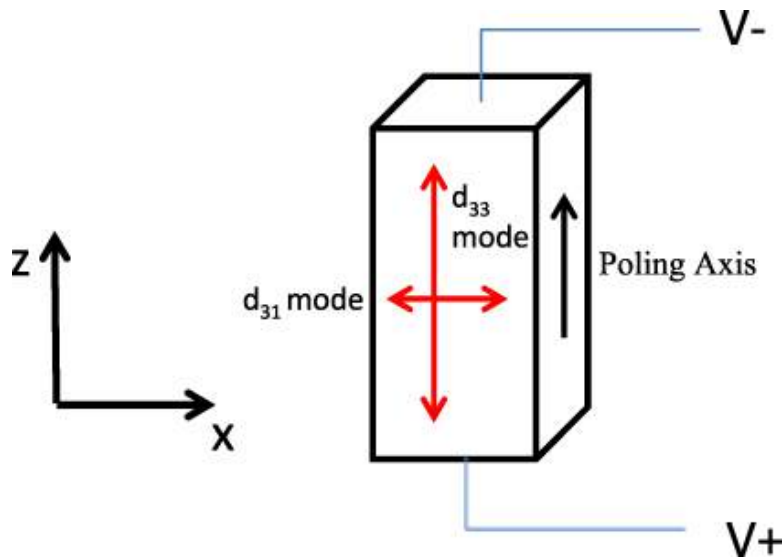


Figure 1.5. Actuation direction for d_{31} and d_{33} mode (Tolliver et al., 2013)

Figure 1.6 shows the d33 configuration for the MFC, which is mainly used for actuation due to the fact the elongation can reach up to 1800 ppm. Figure 1.7 shows the d31 configuration, which is mainly used for energy harvesting and strain sensing. The d31 configuration can only contract up to 750 ppm. For the purposes of this work, the d33 configuration will be used due to the higher actuation deflection potential.

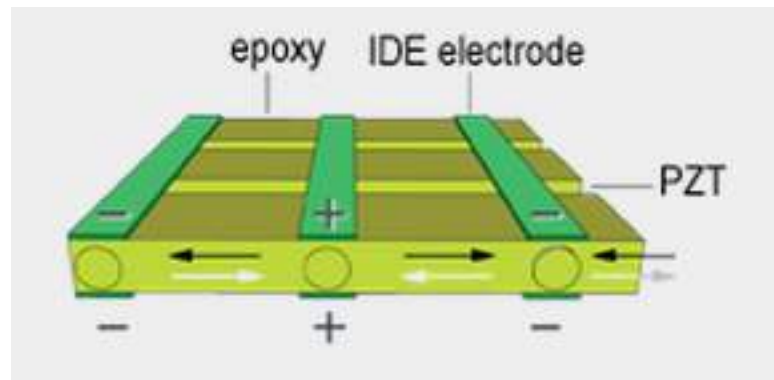


Figure 1.6. d33 configuration for MFC (Smart-Material, 2015)

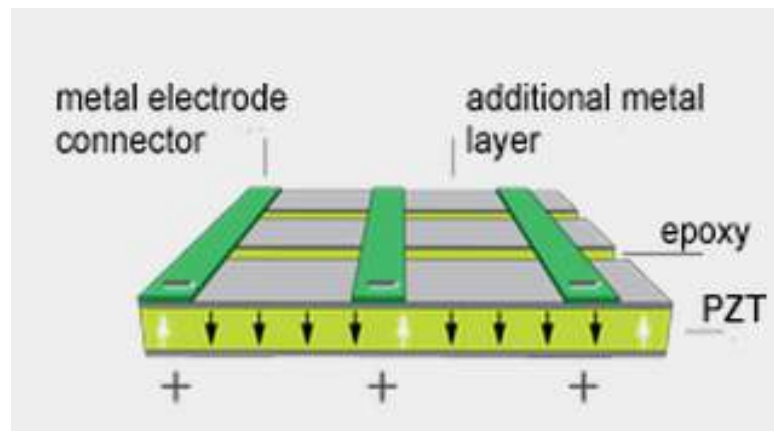


Figure 1.7. d31 configuration for MFC (Smart-Material, 2015)

MFCs are commercially available to the public which also makes it a favorable actuator to use as they can be purchased in various sizes. One major advantage

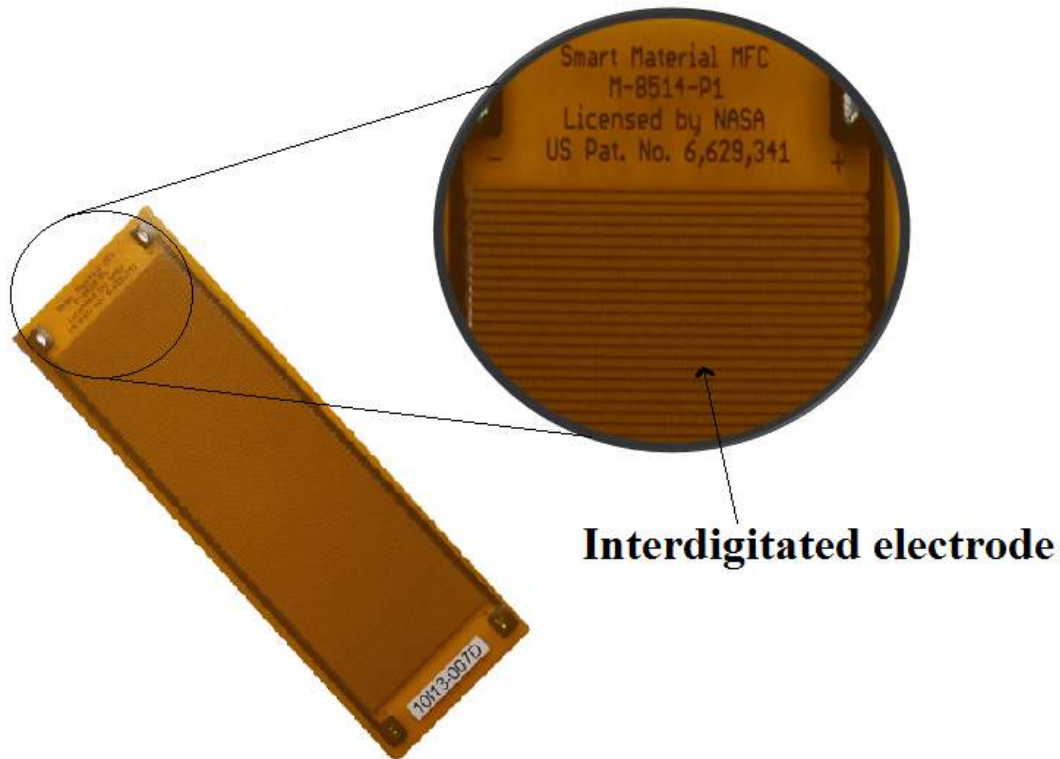


Figure 1.8. M-8514 MFC

of the use of MFC for this specific application is that the MFC is as compliant as the electroadhesion pad as they are roughly 0.3 mm in thickness. They are also lightweight, which is favorable since the goal is to keep the electroadhesion mechanism as small, light, and agile as possible. They also demonstrate great fatigue resistance as the typical lifetime as an actuator is $10E+08$ cycles (Smart-Material, 2015). The operating voltage range for the MFCs used for this work ranges between -500 to +1500 Volts. The MFC type that was used for this application was the M 8514 P1 D33 MFC(figure 1.8). The overall dimensions for each MFC is 101 mm x 20 mm, but the active dimensions (where the piezo actuators lay upon) are 85 mm x 14 mm. This dimension was chosen was so that it would be possible to later attach multiple

MFCs across the electroadhesion pad. The advertised blocking force produced by this specific MFC is 202 N. Blocking force is the maximum force generated by the MFC if actuated against an infinitely stiff wall.

1.3 Research Motivation

The concept of electroadhesion has been used in various industries including space applications. Electroadhesion pads have been developed in various shapes and sizes but there has always been the drawback that the pad must come to almost complete surface contact to obtain optimum adhesion. This is rather difficult especially when the objects to adhere to are of irregular shape and uncertain surface properties. Using composite actuators such as MFCs as will help obtain much better adhesion by allowing higher surface contact, which is the purpose of this thesis.

2. Theoretical Background

2.1 Flat Plate Capacitor Models

In order to better understand the variables that affect electroadhesion force mathematically, we can use calculations set forth for electrostatic forces. Figure 2.1 shows an image the electric field between a parallel flat plate capacitor when subjected to a voltage gradient. It is noticeable that the field vectors have a discontinuity along the plate edge, but remain consistent in the regions between the plates.

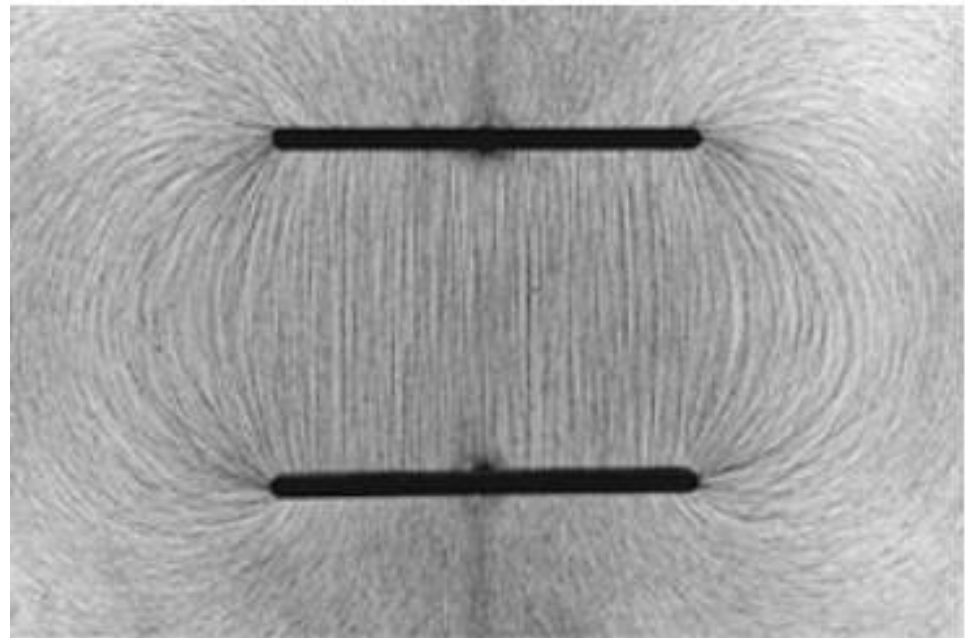


Figure 2.1. Electric field flux for parallel plate capacitor (Busse, 2004)

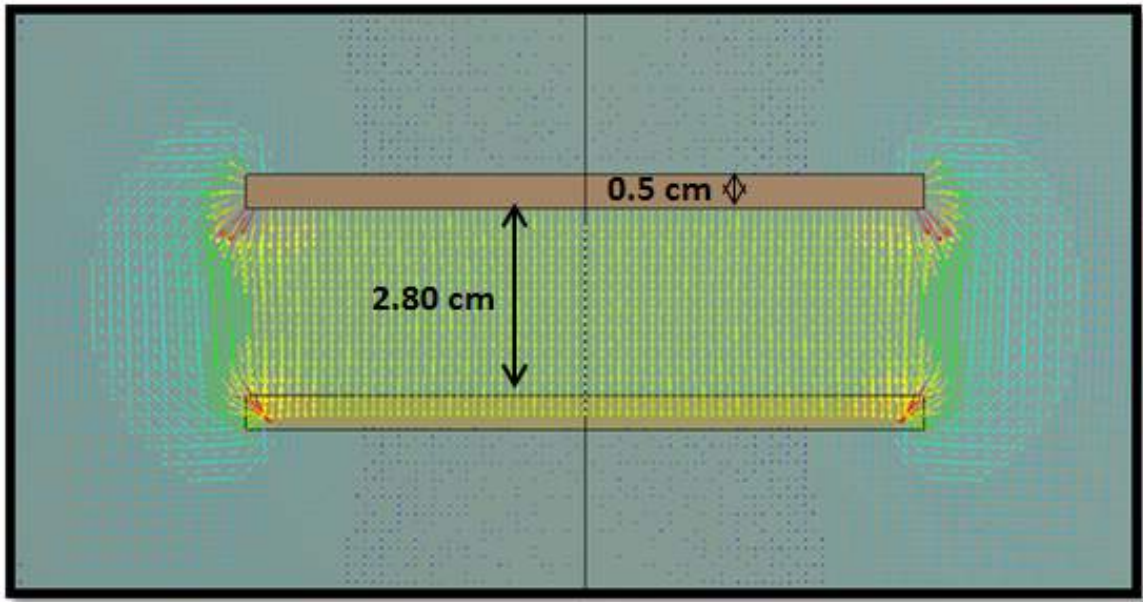


Figure 2.2. Simulation of electric field flux for parallel plate capacitor

Some of the underlying assumptions made for parallel plate capacitor equations is that the electric field between the electrodes is homogeneous and that any end effects are neglected. Figure 2.2 shows a simulation using ANSYS EMag of the electric field distribution lines for a typical flat plate capacitor when energized. The purpose of this simulation was to observe the field behavior of a flat plate capacitor. Notice the end effects on the plate edges where the electric field tends to bow out due to the discontinuity in voltage (as seen in figure 2.1). The regions between the plates tend to be more consistent in how the field behaves under a voltage gradient. Electrostatic forces can typically be calculated using two known methods (Losonc, 2015). The first one described in this section is the direct method, which is based on Coulomb's law.

The second method described in an indirect method based on the energy conservation law.

2.1.1 Coulomb's Law (Direct Method)

Equation 2.1 describes the relationship between electrostatic force, charge, and electric field. It is shown that the force generated is a function of the electric field, which will be discussed in more detail later.

$$F = qE \quad (2.1)$$

Equation 2.2 shows the force density equation (force per surface area of the plate).

$$f = \frac{\sigma^2}{2\epsilon} \quad (2.2)$$

The voltage gradient U is defined as the difference between the voltages on the plates.

$$U = V_2 - V_1 \quad (2.3)$$

The electric field can be expressed as the charge density over permittivity as shown in equation 2.4 and more traditionally can be expressed simply as the voltage gradient divided by the distance between the plates (equation 2.5).

$$E = \frac{\sigma}{\epsilon} \quad (2.4)$$

$$E = \frac{U}{l} \quad (2.5)$$

Equation 2.4 can be rearranged to solve for σ as shown in equation 2.6. Equation 2.5 can further be substituted into equation 2.6, which results in equation 2.7.

$$\sigma = \varepsilon E \quad (2.6)$$

$$\sigma = \frac{\varepsilon U}{l} \quad (2.7)$$

Substituting equation 2.7 into equation 2.2 helps describe the force density as a function of permittivity, voltage, and plate gap (equation 2.8). Multiplying the force density by the surface area (S) will result in the resultant electrostatic force as shown in equation 2.9.

$$f = \frac{\varepsilon U^2}{2l^2} \quad (2.8)$$

$$F = \frac{\varepsilon U^2 S}{2l^2} \quad (2.9)$$

2.1.2 Energy Conservation Law (Indirect Method)

This method assumes the validity of energy preservation and derives the forces from energy correlations. Equation 2.10 shows the force as a function of the energy stored between the capacitors. Energy can be showed as a function of charge and

voltage (equation 2.11). Since charge is defined as capacitance times voltage, equation 2.12 can be used to represent the energy stored.

$$F = \left| \frac{dW}{dl} \right| \quad (2.10)$$

$$W = \frac{QU}{2} \quad (2.11)$$

$$W = \frac{CU^2}{2} \quad (2.12)$$

Capacitance can be described mathematically as equation 2.13, and can be substituted into equation 2.12 to result in the energy as a function of permittivity, surface area, voltage, and plate distance (equation 2.14).

$$C = \frac{\varepsilon S}{l} \quad (2.13)$$

$$W = \frac{\varepsilon SU^2}{2l} \quad (2.14)$$

As previously shown in equation 2.10, the change in energy with respect to plate distance is equal to the force, which results in equation 2.16. Equation 2.16 calculated through energy conservation law matches that of equation 2.9, which was calculated using Coulomb's law.

$$\frac{d}{dl} W = -\frac{\varepsilon SU^2}{2l^2} \quad (2.15)$$

$$F = \frac{\varepsilon S U^2}{2l^2} \quad (2.16)$$

2.2 Electric Field in Electroadhesion Applications

Electroadhesion pads consist of at least two electrodes that are embedded within a dielectric medium that is used as the insulator. Electroadhesion is achieved in different manners depending on whether the substrate (the material it is adhering to) is a conductor or an insulator (Germann, 2014). When the electroadhesion pad is adhering to a conductive substrate, electric fields are generated between both electrodes which attract free charges. Opposite charges start to form under the electrodes which create the attractive force to the substrate. When the electroadhesion pad is adhering to a non-conductive substrate, the attraction force is generated through polarization of the substrate caused by the electric field. Electric fields are generated between the electrodes and use the insulator as a medium of field transportation. The force is proportional to the square of the electric field between the electrodes and the substrate (Parness, 2013).

Essentially, for conductive substrates, the electric fields will be concentrated mostly below the electrodes as illustrated in Figure 2.3. For an insulator substrate, the electric fields will be concentrated mostly in the regions between the electrodes as illustrated in Figure 2.4. The electric fields created when a voltage gradient is present results in normal and shear adhesion forces between the pad and the adhering substrate surface.

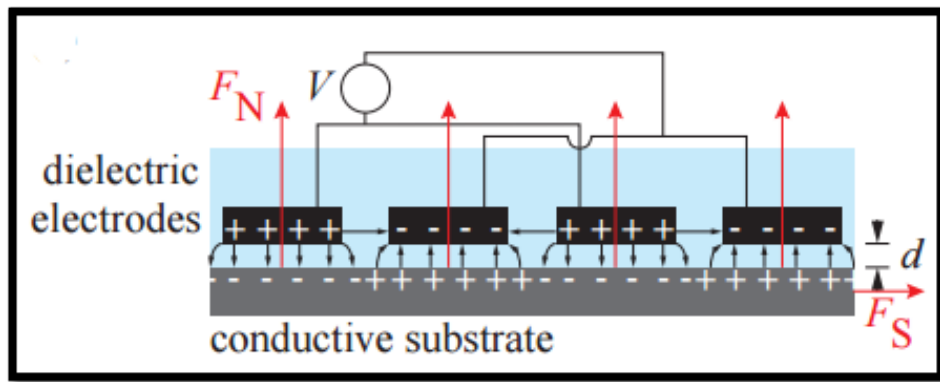


Figure 2.3. Formation of Opposite Charges on Conductive Surface (Germann, 2014)

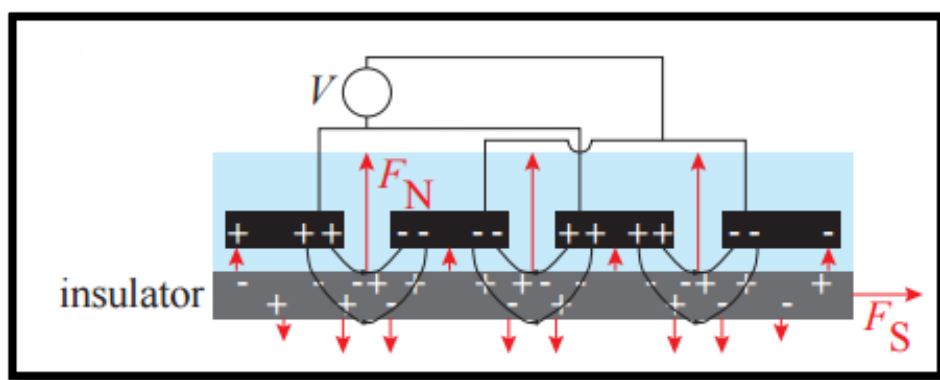


Figure 2.4. Polarization Between Electrodes on an Insulator Surface (Germann, 2014)

As seen in equation 2.1, the electric field plays a crucial role in the amount of adhesion generated. Theoretically, the higher the electric field, the higher the adhesion force will be. Therefore, we would want to minimize the gaps between the electrodes in order to increase the electric field, but this can lead to potential dielectric breakdown. Dielectric mediums, including any air gaps, have a corresponding dielectric strength for any specific thickness. The dielectric strength of an insulator is defined as the ultimate value of electric field that can be applied without irreversible damage.

age, such as dielectric breakdown (*Inductors and transformers for power electronics*, 2015). Once dielectric breakdown occurs of a material, the path that broke down becomes conductive and the electric field is disrupted. This results in an failed pad since little to no adhesion will be present after dielectric breakdown.

Referring back to the parallel plate capacitor in section 2.1, the electric field can be calculated using Gauss' law. Gauss' law is a universal law that describes electricity. It is described as

$$\phi = \oint \vec{E} \cdot d\vec{S} = \frac{q_{enc}}{\epsilon_0} \quad (2.17)$$

where the integral of the electric field vectors over a surface area equals the resultant electric flux (Dourmashkin, 2004). This is also equal to the charge enclosed between the plates divided by the permittivity of space. With defined parameters, equation 2.17 can be re-written as

$$ES' = \frac{q_{enc}}{\epsilon_0} \quad (2.18)$$

$$q_{enc} = \sigma S' \quad (2.19)$$

Substituting equation 2.19 into 2.18 yields

$$E = \frac{\sigma}{\epsilon_0} \quad (2.20)$$

Charge density will vary when dealing with irregularly shaped geometries due to the voltage distribution varying along the electrodes. Due to the complex shapes of the electrodes, it is more efficient to perform electrostatic finite element analysis in order to determine the field magnitude and distribution across the electrodes. Determining the electric fields also ensure a proper safety factor is acquired in order to reduce the probability of dielectric breakdown.

One of the initial electroadhesion pads that was fabricated consisted of spiral electrode designs that had a very small gap distance between the electrodes (0.9 mm). Although the electrostatic FEA showed that no dielectric breakdown was predicted on the insulation, breakdown occurred on the pad during testing at 3,000 V. This was due to air gaps that were trapped between the electrodes when overlaying the outer Kapton tape layer. The air gaps trapped between the electrodes formed a high stress gradient (stress concentration) that caused ionization and caused the insulation break down. Figure 2.5 shows the tested spiral pad after dielectric breakdown was observed.

The region pointed with the red arrow is the location that the breakdown occurred. In order to mitigate this potential issue, the gaps between the electrodes were increased so that the possibility of trapping air pockets was reduced while applying the outer insulation tape.

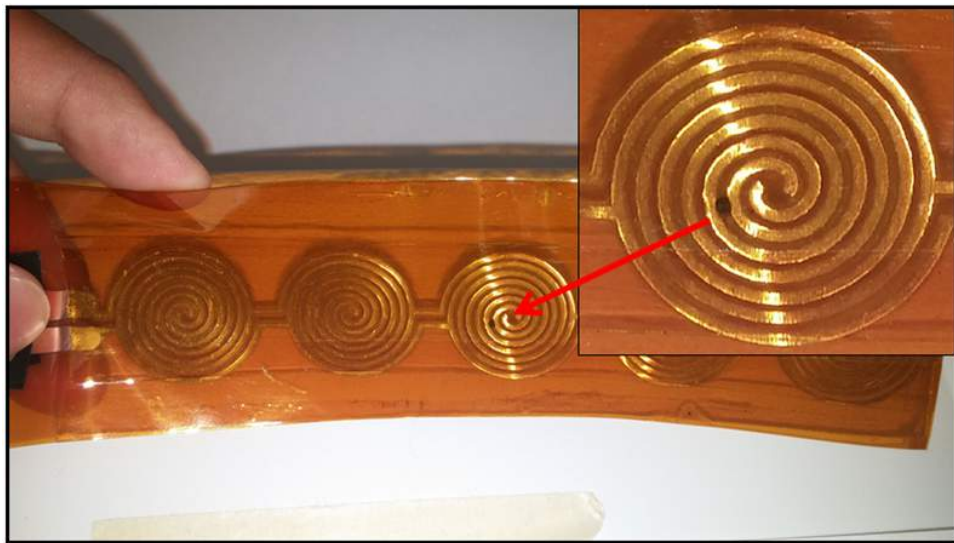


Figure 2.5. Dielectric Breakdown of a Spiral Pad Design

2.3 MFC calculations

There are multiple variables that determine the amount of deflection a substrate will endure due to actuation from an attached MFC. The main variables that affect the deflection is the material of the substrate, the thickness of the substrate, the thickness and width of the MFC, and the blocking force of the MFC. There are some variables that are quite difficult to treat analytically such as the bonding method and whether the MFC is clamped on one end like a cantilever beam.

There are two types of configurations available for MFC attachment on a substrate; unimorph or bimorph (Prazenica, 2014). A unimorph design consists of a substrate material with an MFC(s) attached to only one side. A bimorph design also consists of a substrate, but with an MFC(s) attached to both sides which allows greater deflection on both sides of the pad. Since the application of the electroadhesion pad requires

the adhering side to be smooth in order to allow max adhesion, a unimorph MFC design was chosen.

The deflection of a unimorph assembly that is fixed along one end (similar to a cantilever beam) can be calculated analytically as shown below (Prazenica, 2014).

$$\delta = -\frac{F_b L^3}{3wD_1} \quad (2.21)$$

$$D_1 = \frac{E_s^2 t_s^4 + E_{MFC}^2 t_{MFC}^4 + 2E_s E_{MFC} t_s t_{MFC} (2t_s^2 + 2t_{MFC}^2 + 3t_s t_{MFC})}{12(E_s t_s + E_{MFC} t_{MFC})} \quad (2.22)$$

$$F_b = \frac{3wE_s t_s E_{MFC} t_{MFC} (t_s + t_{MFC})}{4L(E_s t_s + E_{MFC} t_{MFC})} d_{33} E_3 \quad (2.23)$$

$$E_3 = \frac{V_{applied}}{t_{MFC}} \quad (2.24)$$

2.3.1 Theoretical Calculations

Using material properties for the M-8514 MFC(Smart-Material, 2015) and the LF9130 Pyralux (DuPont, 2012), deflections were calculated in order to estimate the expected deflection of the MFC. The dimensions assumed for the MFC are 101 mm length, 20 mm width, and 0.3 mm thick. The thickness of the electroadhesion substrate is assumed 0.3 mm. A voltage of 1,500 Volts was assumed.

Solving for equation 2.21 resulted in a calculated deflection of 2.3 cm. When the MFC was attached to the electroadhesion pad for testing, the MFC was actuated

and the deflection of the assembly was recorded. The deflection at the tip of the pad was approximately 2.54 cm. which results in a percent difference of 9.9%. The percent difference is most likely due to the fact that in the calculations, we assumed the Pyralux substrate is not etched, which affects the stiffness of the composite due to the geometry of the electrodes. The calculation still gave a good approximation of what deflection to expect on the pad when actuated with the MFC.

3. Design of Electroadhesion Pad

3.1 Design Requirements

The equations from Chapter 2 show that the magnitude of electrostatic force is a function of the electrode surface area, the applied voltage, and distance between the electrodes. The electrode surface area and the distance between the electrodes have been the two main variables adjusted during the design of the pads. Since the goal is to use the pads in space, it was important to keep the size as compact as possible for packaging while still being able to adhere to potential objects found in low earth orbit. Preliminary studies of orbit operations show that the maximum required force per pad is on the order of a few tens of Newtons (Udrea, 2015). For now, the optimization of the pad geometry was the main focus as the sizes could later be scaled higher or lower depending on the required adhesion levels for specific missions.

The geometries of the electroadhesion devices can vary significantly based on the design constraints and requirements since the electrodes can be easily increased in size to achieve higher adhesion levels. The electrode dimensions and sizes play an important role in the amount of potential adhesion that can be obtained. Some studies have been conducted by others in the effect of changing the electrode shape configuration and the size (Ruffatto, 2013). In Chapter 2, it is shown mathematically that reducing the distance between the electrodes results in higher adhesion. Theoreti-

cially, it would make sense to design the distance between the electrodes as small as one can fabricate. The arising issue is that as the gap between electrodes decreases, the electric field increases, which can potentially break down the insulating medium as shown in figure 2.5. It is important that no dielectric breakdown occurs within the insulation, otherwise it will cause the system to short out and reduce or eliminate the adhesion performance of the pad. Figure 3.1 shows some of the designs that have been created, analyzed, and tested by other researchers in order to compare adhesion between various geometric configurations (Ruffatto, 2013).

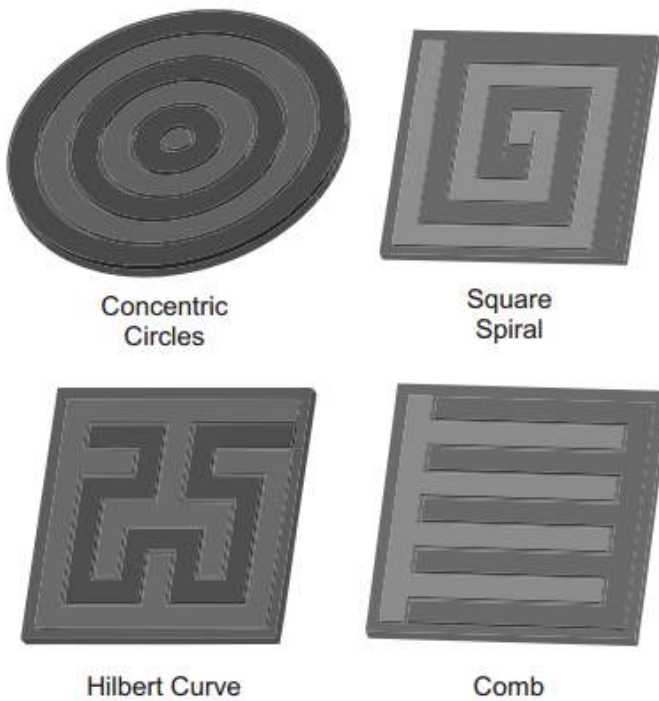


Figure 3.1. Example of pad designs created by other researchers (Ruffatto, 2013)

Out of the four designs, it was shown by the testing of the researchers that the concentric circles and comb designs resulted in highest adhesion. For the research

discussed here, a variety of different electrode shapes and sizes were also designed and tested to determine the optimized geometry that provides highest adhesion within the design constraints.

Multiple pad designs were created in CAD in order to filter out the best design based on the electrostatic finite element analyses and the feasibility of fabrication. It is planned to have the electroadhesion pad serve as a gripping mechanism that can conform not only to a wide variety of materials, but also to a wide variety of surface shapes. Maximum adhesion occurs when the pad has perfect contact with the surface it is adhering to. In reality, perfect contact is highly unlikely or even impossible due to the variation in surface finishes. For surfaces with curvature, it is necessary to have an actuation method embedded in the electroadhesion pad.

Figure 3.2 shows the schematic of the non-actuated electroadhesion pad concept that consists of strain gages and actuators. The pad is essentially composed of a compliant dielectric material with embedded electrodes that allow voltage to travel through the length in order to create electroadhesion. Actuators (yellow bodies) and strain gages(blue bodies) are also used to create a closed loop active feedback system. The strain gages are used to determine the curvature of the pad.

As the electroadhesion pad approaches close proximity of the debris surface and makes initial contact, the strain sensors will determine the areas of curvature and will provide active feedback for the actuators in order to deflect the electroadhesion pad. Actuating the electroadhesion pad in order to increase the contact area between the pad and debris surface will increase the magnitude of adhesion. Figure 3.3 shows the

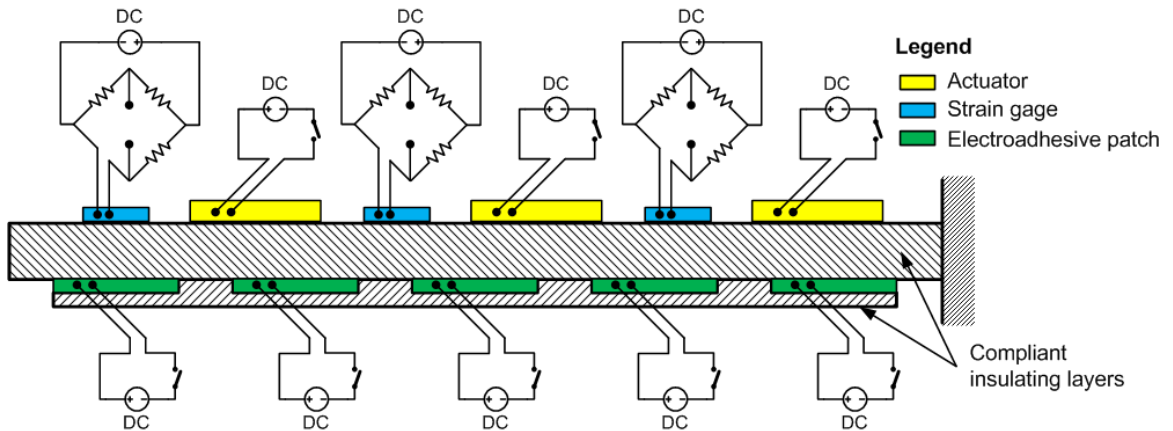


Figure 3.2. Schematic of Non-actuated Electroadhesion Pad

schematic of an actuated electroadhesion pad. It is planned to eventually have an independent actuator system so that only portions of the pad are actuated based on the shape of the surface with which contact is made.

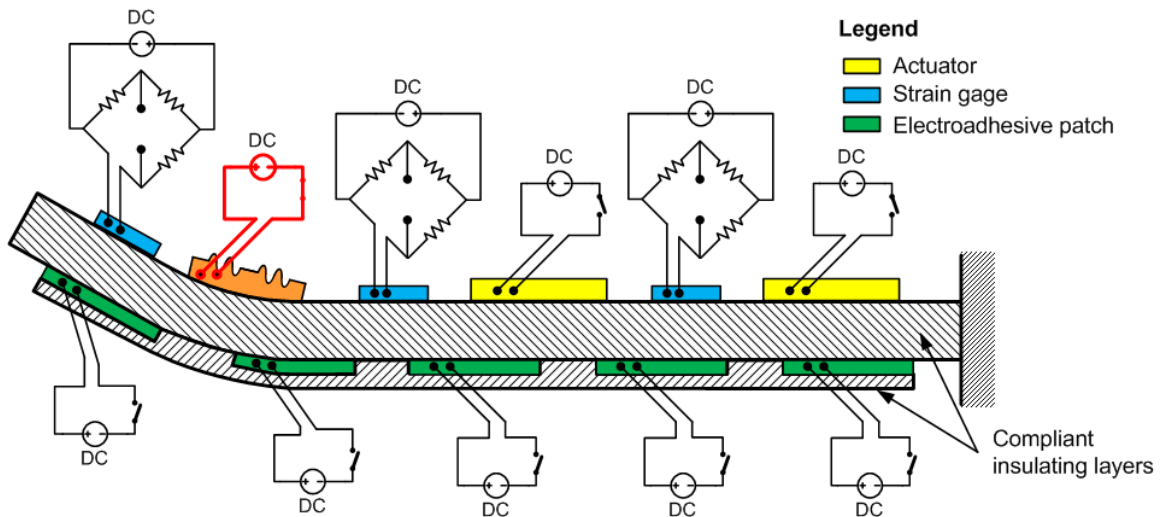


Figure 3.3. Schematic of Actuated Electroadhesion Pad

3.2 Finalized Designs

Preliminary mission designs show that a pad size of 20 x 5 cm is most likely to be used. All the pad geometries were created in SolidWorks CAD software. Parametric features were created on the pad geometries in order to easily adjust the thickness of the electrodes or dielectric thickness. Parametric features were also created on the distance between the electrodes. Another design constraint which is derived from manufacturability considerations is that the pad is fabricated from Pyralux. The Pyralux composites are available only in certain thicknesses, therefore, the thickness of the pads is based on the availability from the supplier. All the finalized models consist of a 0.076 mm thick polyimide layer which is assuming the use of Pyralux LF9130(DuPont, 2012).

Figure 3.4 shows the finalized design of the spiral electroadhesion pad, which measures 19 cm in length and 4.3 cm in width. The gap between the electrodes is a nominal 0.19 cm, and the total electrode surface area is 35.3 cm^2 . The geometry was designed in such a way that if needed, each spiral set could be set up as an independent circuit where voltage would be applied to a spiral only where needed. For this research, the spirals are part of continuous circuits. A pair of straight leads were created on the left side in order to allow room for soldering the electrical wires.

Figure 3.5 shows the finalized design for the four tooth comb design, in which the electrode measures 14.3 cm in length and 3.5 cm in width. The gap between the

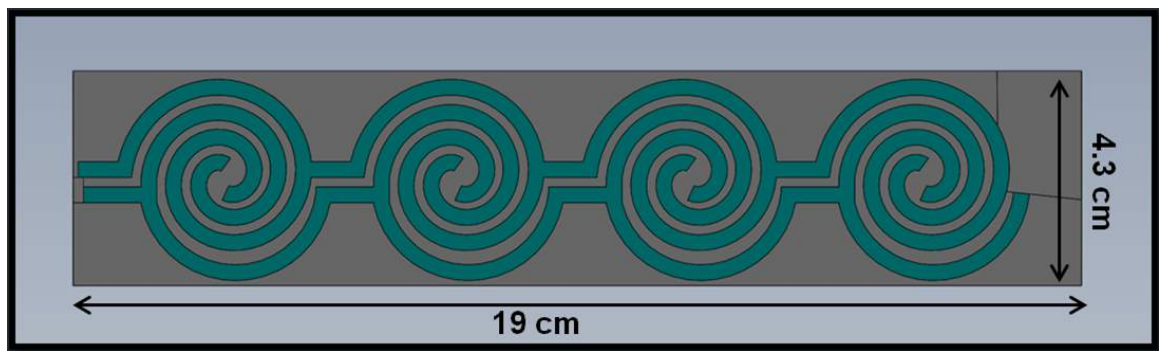


Figure 3.4. Dimensions of Spiral Pad Design

electrodes is 0.5 cm, and the total electrode surface area is 33.7 cm^2 . Soldering leads were incorporated on each side in order to allow easy solder ability.

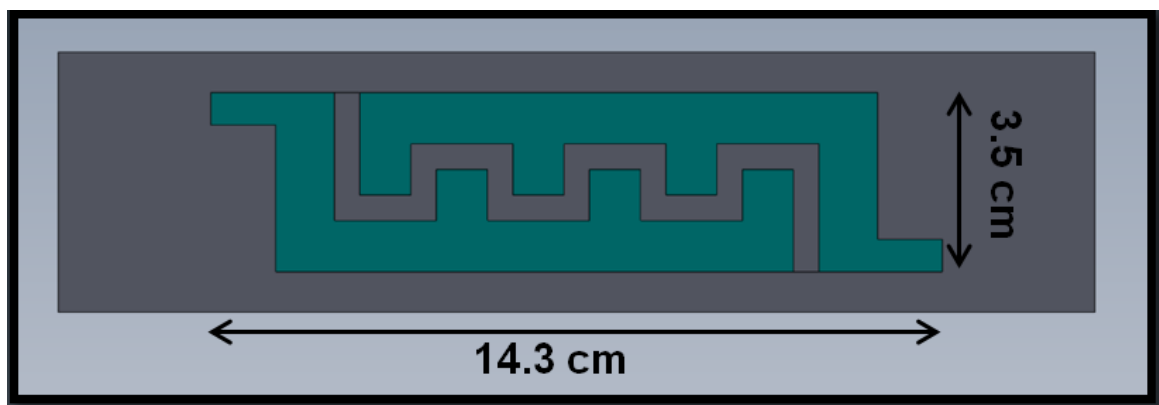


Figure 3.5. Dimensions of Four Tooth Pad Design

Figure 3.6 shows the finalized design for the eight tooth comb design, in which the electrode measures 18.2 cm in length and 2.6 cm in width. The gap between the electrodes is 0.5 cm, similar to the four tooth pad design, and the total electrode surface area is 29.6 cm^2 . The pair of solder leads were added on the left side of

the pad. It is important to assure that the soldering ends are not in too close of proximity. If they are too close when energized and if not properly insulated, then tracking between electrodes can occur, which results in a short circuit.

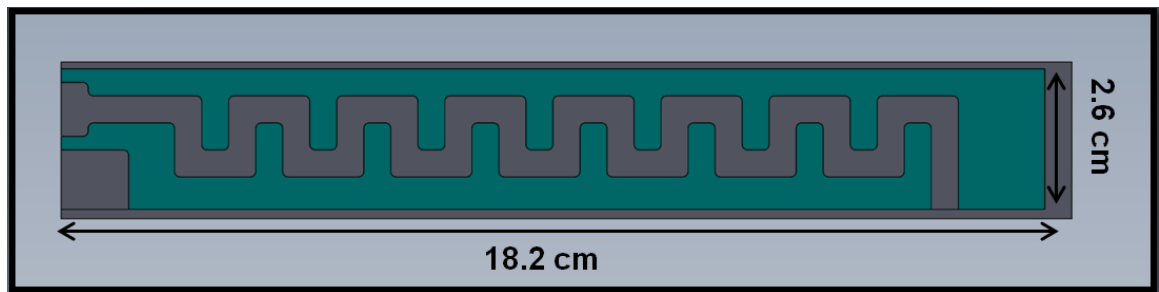


Figure 3.6. Dimensions of Eight Tooth Pad Design

The three designs mentioned above were chosen as the main candidates in order to pursue further analysis, fabrication, and testing.

4. Finite Element Analysis

In this chapter, the numerical analysis of the electric field for the electroadhesion pads is discussed. Models were created through finite element methods in order to calculate the electrostatic behavior of the pads when energized.

Table 4.1. Environment Within Various Physics Domains Relating to Hooke's Law

Domain	Action [F]	Property [K]	Behavior [u]
Structural	force	stiffness	displacement
Thermal	heat source	conductivity	temperature
Fluid	body force	viscosity	velocity
Electrostatic	charge	dielectric permittivity	electric potential

Complex geometries are efficiently handled via finite element methods and a wide variety of physics domains can be simulated. Hooke's law $F=[K]\{u\}$ (Clark, 2009) can be used as a simple representation of the variables and effects within the finite element method based on different physics domains as seen in Table 4.1. When a charge is created within a dielectric (due to input voltage), an electric potential (which creates electric fields), exists and is determined by the permittivity of the insulation.

4.1 Purpose

The purpose of performing electrostatic FEA on the electroadhesion pads was so that a comparison could be made on the electric field values between the multiple pads designed. Also, validation of the dielectric breakdown safety factor was to be completed before fabricating and testing commenced. As discussed earlier in Section 2.2, when generated electric fields surpass the dielectric strength of an insulation layer, breakdown occurs. Not only is this detrimental to the pad and its adhesion properties, but it can lead to hazardous shock to the person performing testing if proper personal protection equipment (PPE) is not worn.

Electrostatic FEA is a very useful tool in determining electric fields on components with complex geometries, by solving Maxwell's equations (*Partial Differential Equations and the Finite Element Method*, 2005). The first step is to identify the governing equations set forth for electrostatic calculations (Muniraj, 2011). A common way to determine the final electric field distribution is to subtract the gradient of electric potential distribution from the initial field distribution, which is shown in equation (4.1).

$$E = -\nabla V \quad (4.1)$$

which can be also expressed as equation (4.2) by expanding the divergence operator

$$E = \frac{\partial V_x}{\partial x} - \frac{\partial V_y}{\partial y} - \frac{\partial V_z}{\partial z} \quad (4.2)$$

From Maxwell's equation

$$\nabla E = \frac{\sigma}{\epsilon} \quad (4.3)$$

Substituting equation (4.3) into equation (4.1) results in Poisson's equation (equation 4.4)

$$\nabla^2 V = -\frac{\sigma}{\epsilon} \quad (4.4)$$

By making the charge density $\sigma = 0$, Laplace's equation is obtained as shown in equation (4.5), which is the governing system equation used in the formulation

$$\nabla^2 V = 0 \quad (4.5)$$

Assuming a two dimensional Cartesian coordinate system, function $F(v)$ where v is the electric potential can be written as equation (4.6)

$$F(v) = \frac{1}{2} \iint [\epsilon_x (\frac{dv}{dx})^2 + \epsilon_y (\frac{dv}{dy})^2] dx dy, \quad (4.6)$$

where ϵ_x and ϵ_y are the x and y components of the material permittivity. A typical assumption made for common dielectrics is that the permittivity is isotropic ($\epsilon = \epsilon_x = \epsilon_y$). This allows equation (4.6) to be rewritten as equation (4.7), which represents the integral form equation used in the FEM formulation.

$$F(v) = \frac{1}{2} \iint \epsilon |\nabla v|^2 ds \quad (4.7)$$

The next step in the FE solution is to discretize the solid bodies into elements. This is essentially the meshing step where element types are defined and created for the bodies of interest. The next step is to create an approximation of the electric field variable over each element, which is shown in equation (4.8). A first order approximation is defined inside the sub-domain where the field vectors in the x and y directions are dependent of v .

$$v_e(x, y) = a_{e1} + a_{e2}x + a_{e3}y; \quad (e = 1, 2, 3...m) \quad (4.8)$$

where $v_e(x, y)$ is the electric potential of any point, a_{e1} , a_{e2} , and a_{e3} are computational coefficients for each element e , and m is the total number of elements in the sub-domain. The matrix expression for the evaluation of each element in integral form is shown in equation (4.9).

$$[S_{ij}]^e \{v_i\}^e = \{q_j\}^e \quad i, j = 1, 2, \dots, k \quad (4.9)$$

Where k is the total node count in the domain. When assembling the matrices from equation (4.9) into a global matrix equation, we result in

$$[S_{ij}]\{v_i\} = \{Q_j\} \quad i, j = 1, 2, \dots, k \quad (4.10)$$

where $[S_{ij}]$ is the global stiffness matrix that is essentially comprised of the material permittivity values. $\{v_i\}$ is the unknown electric field potential matrix and $\{Q_j\}$ is the free charge matrix, which is based on the applied voltage gradient. Rearranging equation (4.10) in order to solve for the unknowns results in equation (4.11) which is the matrix equation in final form. This is solved for iteratively for each element in the system in order to interpolate the electric field across the domain.

$$\{v_i\} = [S_{ij}]^{-1}\{Q_j\} \quad i, j = 1, 2, \dots, k \quad (4.11)$$

4.2 Methodologies

A finite element analysis can typically be split into three separate stages; pre-processing, processing (solution solve), and post-processing(Gokhale, 2008).

4.2.1 Pre-processing

Pre-processing consists of setting up the model before it is solved computationally. For analyses performed in this thesis, the CAD models were created using SolidWorks CAD program. Once the solid models were created, they were imported into ANSYS FEA software in order to perform the electrostatic analysis. One of the required steps within pre-processing is to define the material properties that will be used for the specific analysis. Since electrostatic analysis was conducted, the material property

needed is the dielectric permittivity of each component. Table 4.2 shows the materials used and their corresponding dielectric permittivity (DuPont, 2012).

Table 4.2. Dielectric Properties of Materials Used for FEA

Material	Dielectric Constant [F]	Dielectric Strength [V/cm]
Polyimide	3.5	2,047,200
Glass	7.6	80,000

Once material properties were created, the components were designated their corresponding materials. The electrodes were modeled as copper and the insulation within the electroadhesion pads were modeled as polyimide. Glass was used as an adhering body material for analyses comparing the electric field on a conductor and insulator surface. Meshing the bodies of study is an important part of the analysis because it can determine how accurate the results are. As in all other numerical analysis methods, the finer the mesh, the higher the accuracy of the results. The drawback to this is that having higher mesh count will result in more computational time and memory. The amount of mesh refinement used for the pads were consistent between the multiple models analyzed. The meshed area of high electric fields, which is the area between the electrodes, was refined to an element size of approximately 0.025 mm in order to obtain higher accuracy. Refer to Appendix A for the details on the mesh density used for all pads in the FEA presented in this research. Since there are two electrodes in each pad assembly, each electrode was assigned a positive

voltage in order to create the electric field gradient. One electrode was setup such that all surfaces are 3,000 Volts, which is the highest voltage used during experimental testing. The other electrode was set as ground, which was to be simulated as ground. Since there is more than one component being analyzed, modeling the contact between the components is also necessary in order to ensure that the electric potential is transferred across bodies. Due to the fact that the Pyralux is fabricated as a composite, it is assumed that there are no air gaps between the copper and polyimide layer. The contacts between the copper and dielectric layers are modeled as fully bonded, ie. adjacent nodes between the bodies are fully transferring the electric potential and that there is no loss of voltage between contact surfaces.

4.2.2 Processing

All simulations were performed on an eight-core desktop system as there was no need to run the analyses on a large cluster. All analyses performed for this thesis converged with no errors. Refer to equations (4.1 - 4.11) for the governing equations used in the processing step of the analysis.

4.2.3 Post-processing

Once a solution has fully converged, the next step involves post-processing the results that were numerically calculated. For electrostatic analysis, the main output of the solution is electric potential across the bodies analyzed. In turn, the electric

field can be further calculated by using the calculated electric potential. As mentioned previously, the main purpose of the analysis was to calculate the electric field. The average surface electric fields between the electrodes were post-processed in order to be able to compare between the pads. The peak electric field was compared against the dielectric strength of the dielectric to ensure that no dielectric breakdown is predicted.

4.3 Assumptions

It is important to understand that performing numerical simulations through the use of FEA results in close approximations based on the amount of assumptions made during the pre-processing stage. There are some considerations that may or may not affect the accuracy of the results, such as environmental effects. It has been noticed that humidity does affect the electroadhesion effects (Sereda, 1965), but the effects of humidity are being ignored for analytical purposes. The material properties were also assumed to be at room temperature ($\approx 22\text{C}$), since this thesis is focused more on the comparison between different pad geometries and the use of MFC. Future work will consist of analyzing and performing experimental tests with varying temperature. The materials being used for the analyses are assumed to have isotropic dielectric permittivities; meaning that the properties are invariant with respect to direction. It has also been assumed that there is no gap between the copper layer and the polyimide layer within the Pyralux composite. In reality, there is a layer of adhesive between both layers measuring $\leq 0.00254\text{ cm}$. The thin layer of adhesive between the copper

and polyimide within the Pyralux composite is being ignored and is assumed to be non-conductive. One of the most important assumptions made is that the contact between the electroadhesion pad and the adhering surfaces are in perfect contact. It is assumed that there is no gap between both bodies. In reality, this is rather difficult or impossible to achieve due to surface imperfections and differences in material finishes or roughness. During experimentation, the EA pads were tested with and without MFCs. The finite element analyses performed assumed that no MFC was attached to the EA pad. This assumption was made due to the fact that the electrostatic analysis was mainly used to compare electric fields between different pad geometries.

4.4 FEA Results

FEA was completed on the various electroadhesion pad configurations, in order to compare the electric field between the configurations and also to calculate the safety factor for the dielectric. A proper safety factor was necessary in order to prevent the probability of dielectric breakdown during testing at 3,000 volts.

4.4.1 Effect of Electrode Gap on the Electric Field

FEA was performed on a four tooth comb pad configuration to compare the effect of electrode gap distance on the electric fields. Figure 4.1 shows the geometry of the four tooth pad with the larger gap between the electrodes, which was modeled as 1 cm. Figure 4.2 shows the geometry with the smaller electrode gap distance of 0.5

cm. The electrode surface areas (31 cm^2) and thickness (0.025 cm) was maintained constant between both models so that the only variable was the electrode distance.

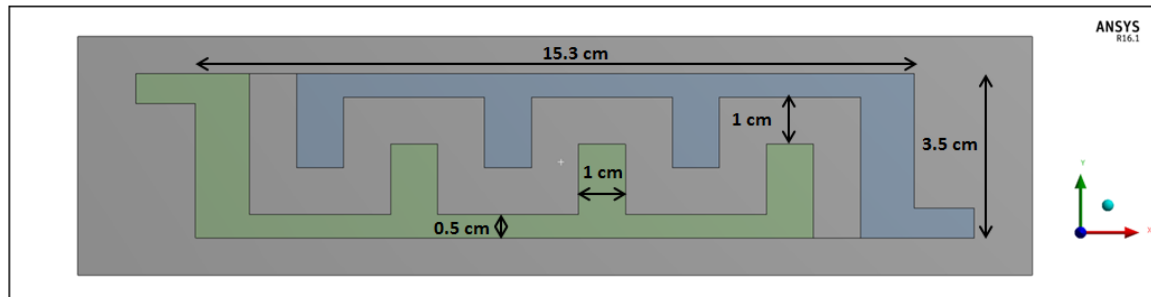


Figure 4.1. Four Tooth Large Gap Model (1 cm gap)

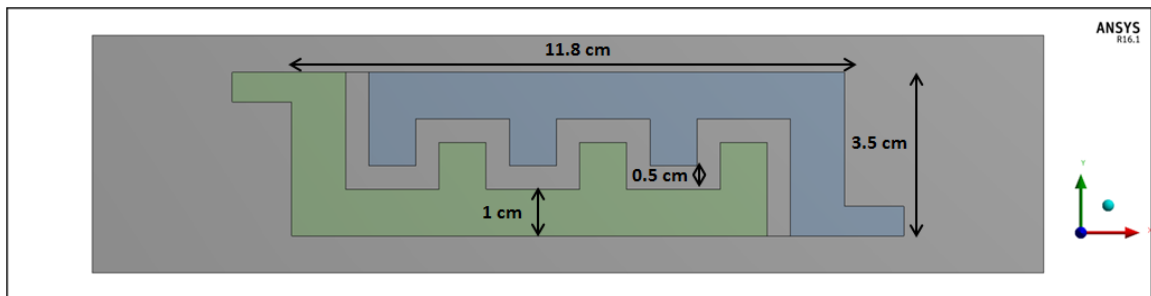


Figure 4.2. Four Tooth Small Gap Model (0.5 cm gap)

Refer to appendix A (figures A.1 and A.2) for the mesh distribution of both pads. As mentioned previously, one electrode has an applied voltage gradient of 3,000 volts, while the other electrode is assumed grounded. Figure 4.3 and figure 4.4 show the voltage distribution of the large gap and small gap pad configuration, respectively. It is observed that the voltage distribution is quite similar between both configura-

tions. As expected, there is a higher voltage gradient per area between the electrodes in the small gap configuration.

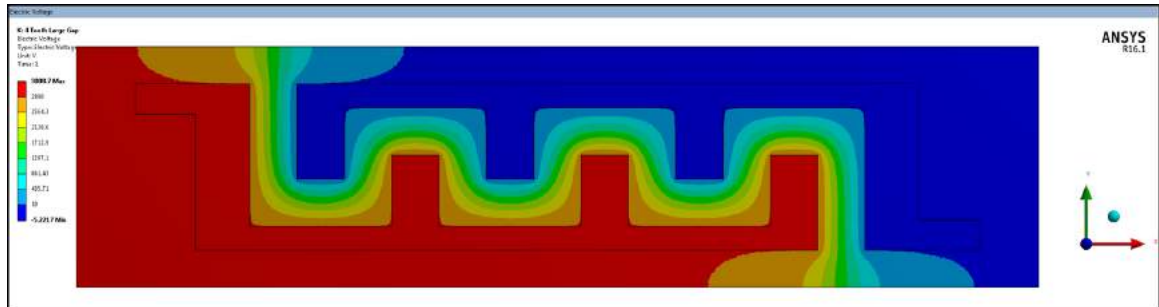


Figure 4.3. Four Tooth Large Gap Voltage Distribution

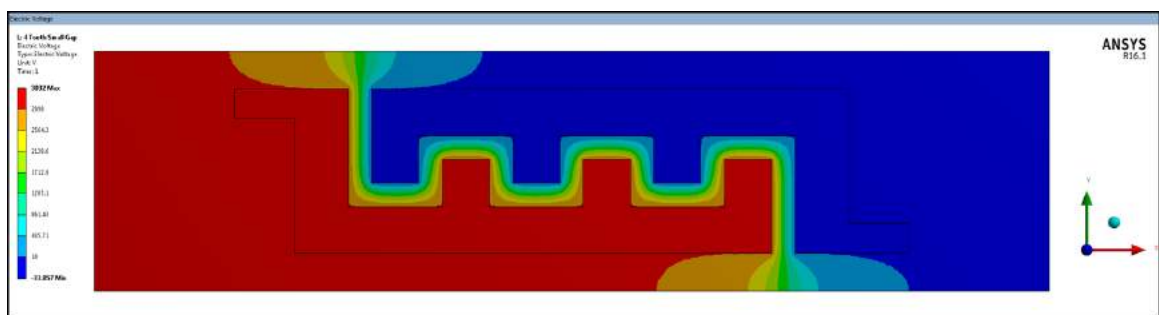


Figure 4.4. Four Tooth Small Gap Voltage Distribution

The main area of interest within the pad assembly is the region between the electrodes. A surface patch was created along the surface between the electrodes in order to post-process the fields within the specific boundary. The electric field color scales are scaled equally in order to compare visually. Figure 4.5 shows the electric field distribution in the large pad configuration. It is observed that the peak fields are

located along the sharp corners of the electrodes. Sharp corners disrupt the smooth transition of voltage flux lines, resulting in localized increase of field stresses. The average electric field between the electrodes was calculated as 2,428 V/cm.

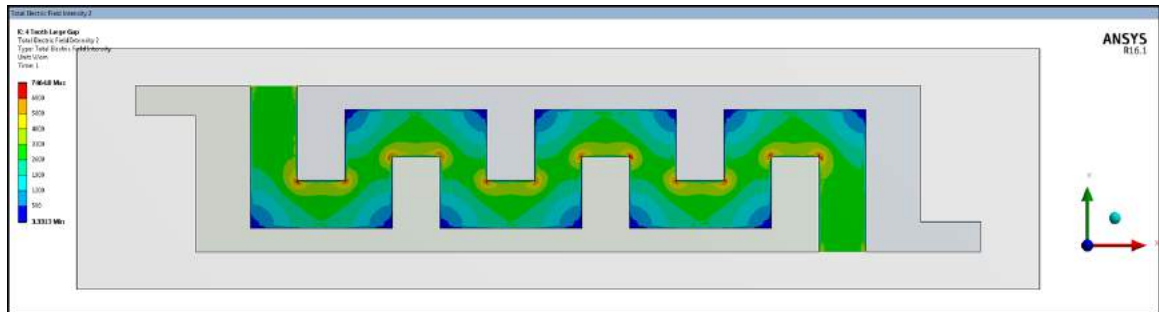


Figure 4.5. Four Tooth Large Gap Electric Field Between Electrodes

Figure 4.6 shows the electric field distribution in the small gap pad configuration. It is observed that there is a significant increase in electric fields when reducing the electrode gap distance by half. The average electric field between the small gap electrodes was calculated as 4,891 V/cm. The percent difference in average electric fields between the configurations is 67%. This analysis comparison shows that the electric field increases as the distance between the electrode gaps decreases, which correlates with the flat plate capacitor equations mentioned in Chapter 2.

4.4.2 Effect of Substrate Thickness on the Electric Field

The effect of the substrate thickness on the electric field was also studied analytically via electrostatic FEA. Analysis was performed on two spiral electrode pad config-

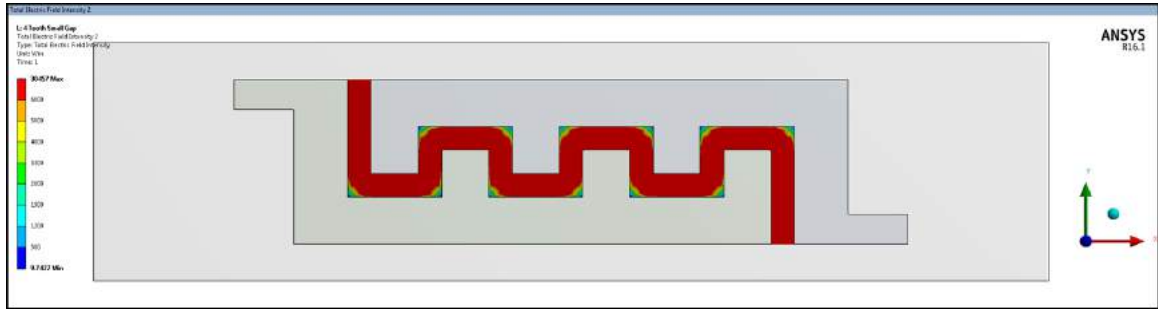


Figure 4.6. Four Tooth Small Gap Electric Field Between Electrodes

urations with different substrate thicknesses. Initially, Dupont's Pyralux LF9120 material was used for experimentation which has a polyimide film thickness of 0.005 cm. Pyralux LF9130, which has a polyimide film thickness of 0.0076 cm was also used. Both configurations were analyzed and compared in order to determine if the additional 0.0025 cm would significantly affect the electric field. Figure 4.7 shows an isometric view of the spiral pad design that was analyzed with the LF9120 and LF9130 configuration. The electrode thickness (blue and green components) for this geometry is 0.0025 cm and the only variable changed was the substrate thickness (gray component). The mesh density is shown in Appendix A, figure A.3.

Figure 4.8 shows the voltage distribution between both electrodes. Again, a 3,000 V gradient was applied between the electrodes. The voltage distribution looked similar between the LF9120 and LF9130 configuration. It is observed that the highest voltage gradient occurs between the electrodes as expected.

A surface patch was created between the electrodes in each assembly model in order to post-process the electric fields. Figure 4.9 shows the electric field distribution

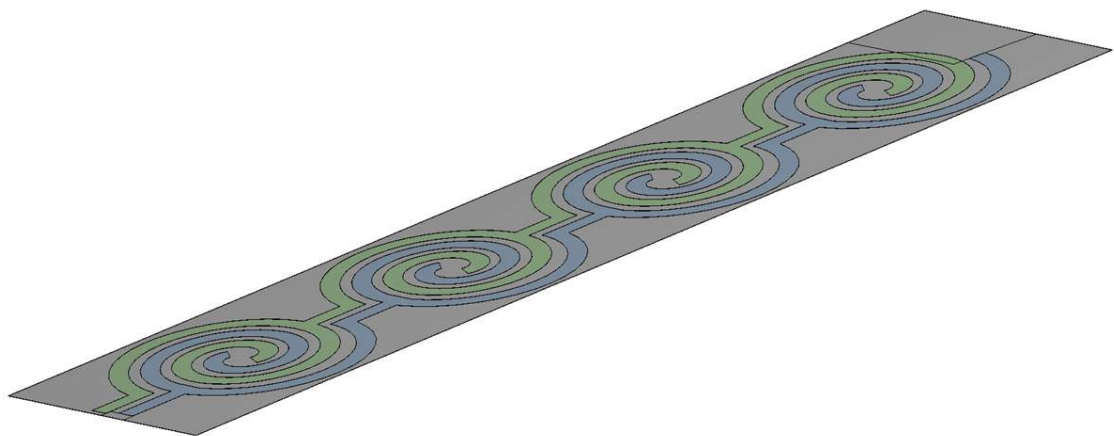


Figure 4.7. Isometric view of Spiral Design

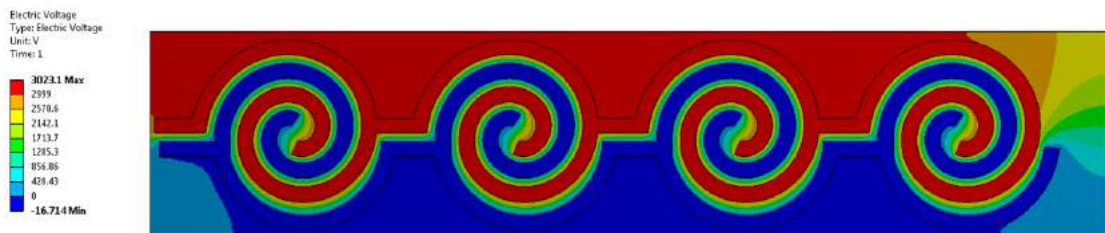


Figure 4.8. Voltage Distribution for Spiral Design

between the electrodes in the LF9120 configuration. Figure 4.10 shows the same electric field distribution plot, but with the LF9130 configuration. Both electric field plots were scaled equally for proper visual comparison.

The average electric field in the LF9120 configuration was 13,290 V/cm. The average electric field in the LF9130 configuration was 13,336 V/cm. The percent difference between both averages is 0.35%. There is very minimal difference in electric

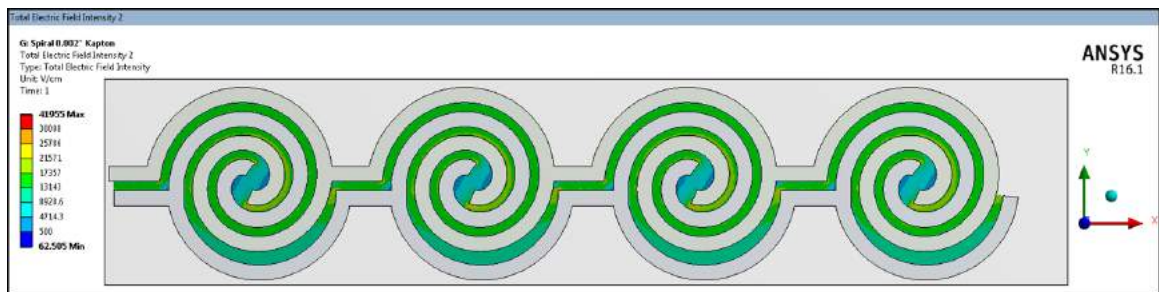


Figure 4.9. LF9120 Electric Field Between Electrodes for Spiral Design

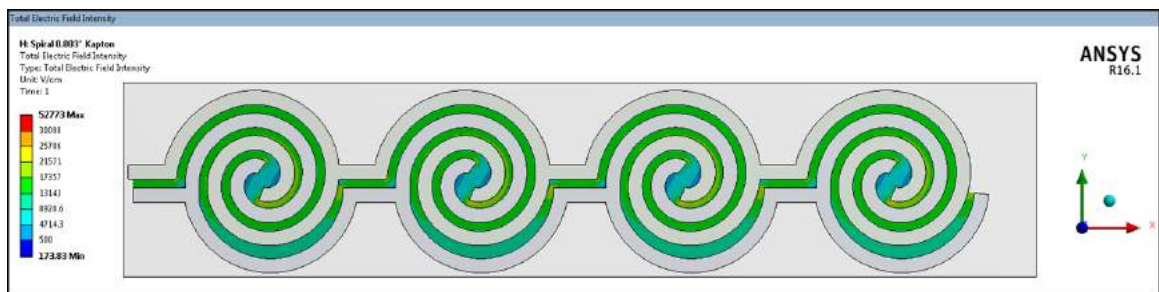


Figure 4.10. LF9130 Electric Field Between Electrodes for Spiral Design

field between both configurations when varying the substrate thickness by 0.0025 cm. It is believed that if the substrate thickness would increase significantly, there would be a more noticeable change in electric field. Based on this analysis performed, insignificant electric field change is calculated between the LF9120 and LF9130 Pyralux configuration.

4.4.3 Spiral Electrode Pad Analysis

The spiral electrode pad design using Pyralux LF9130 was analyzed with a conductive body and an insulator body, separately. 3,000 V was applied for all of the following analytical models.

Figure 4.11 shows the voltage distribution of the assembly when assuming the adhering body is conductive (aluminum). The body, which is representing the aluminum body, is assumed to be grounded on all surfaces. It is observed that since the adhering body is conductive, the highest voltage gradient exists between the positive electrode and the substrate surface (ground).

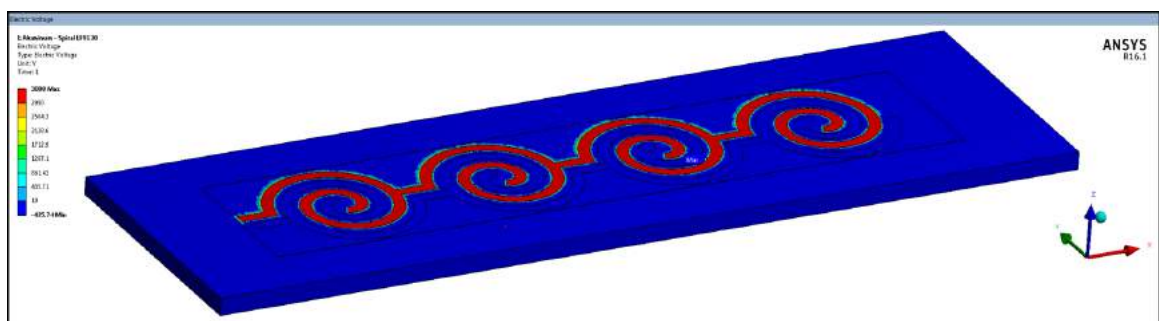


Figure 4.11. Voltage distribution for Conductive Surface

Figure 4.12 shows the electric field distribution in form of vector lines across the assembly. It is observed that the highest electric fields are occurring between the positive electrode and the aluminum surface. An average electric field of 41,571 V/cm is calculated.

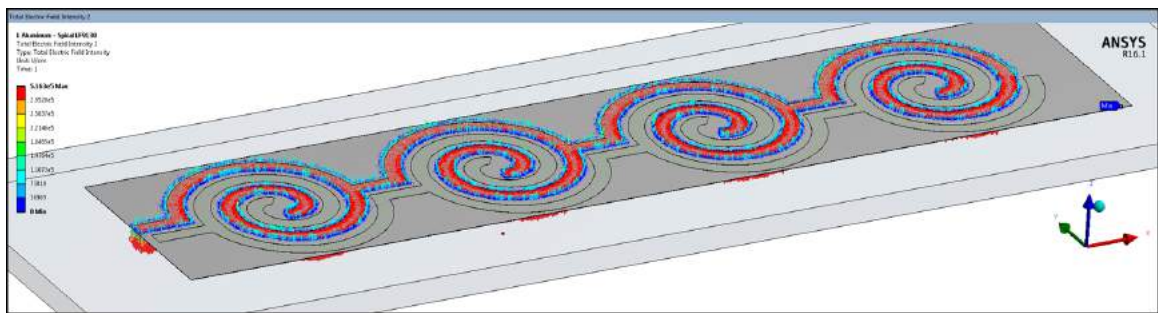


Figure 4.12. Electric Field Between Electrodes for Conductive Surface

Figure 4.13 shows a close up view of the electric field vectors through the thickness of the assembly. It is easier to notice that the field intensity is greatest between the positive electrode and the aluminum surface. As described in the theory section of chapter 2 regarding electroadhesion on conductive surfaces, opposite charges form under the electrodes when energized, which in turn result in high electric fields.

Figure 4.14 shows the voltage distribution of the assembly when assuming the adhering body is an insulator (glass). The insulator body has no applied voltage. It is observed that since the adhering body is an insulator , the voltage gradient is spread throughout the assembly.

Figure 4.15 shows the electric field distribution with vector lines. It is observed that the highest electric fields are occurring between the positive electrode and the negative electrodes. An average electric field of 18,177 V/cm is calculated between the electrodes.

Figure 4.16 shows a close up of the electric field vectors through the thickness of the assembly. It is noticeable that the field intensity is greatest between the posi-

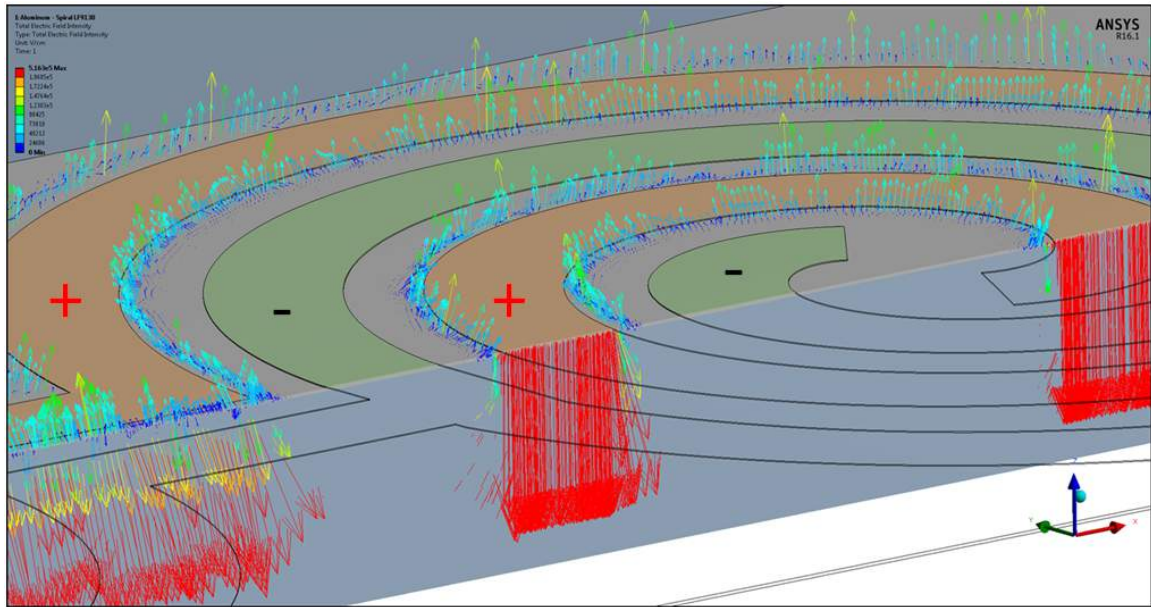


Figure 4.13. Close Up of Electric Field Vectors Under Conductive Surface

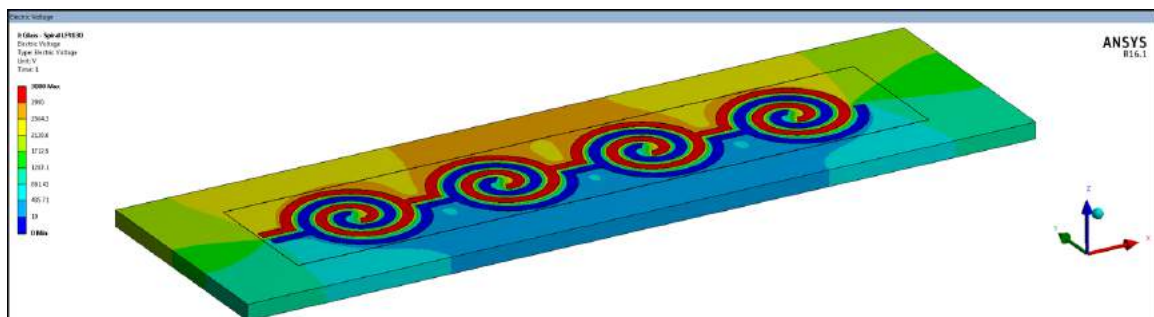


Figure 4.14. Voltage distribution for Insulator Surface

tive and negative electrodes. The field vectors are seen traveling from the positive to the negative electrodes using the glass surface as the medium of transportation. As described in the theory section in Chapter 2 regarding electroadhesion on insula-

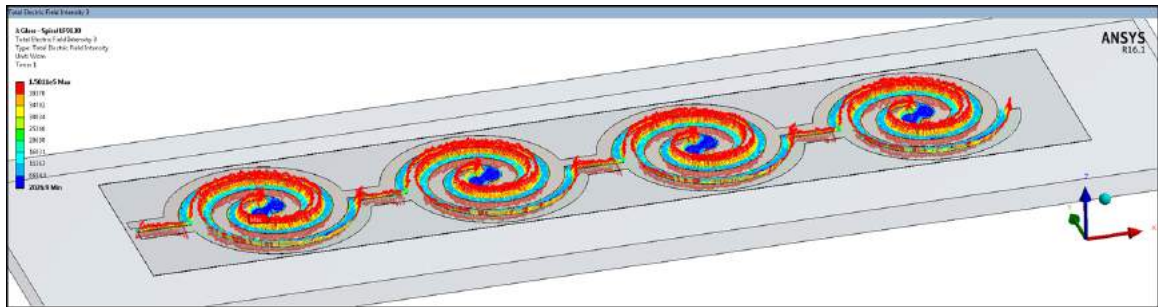


Figure 4.15. Electric Field Between Electrodes for Insulator Surface

tors, polarization is created between the electrodes due to the generated electric field intensities.

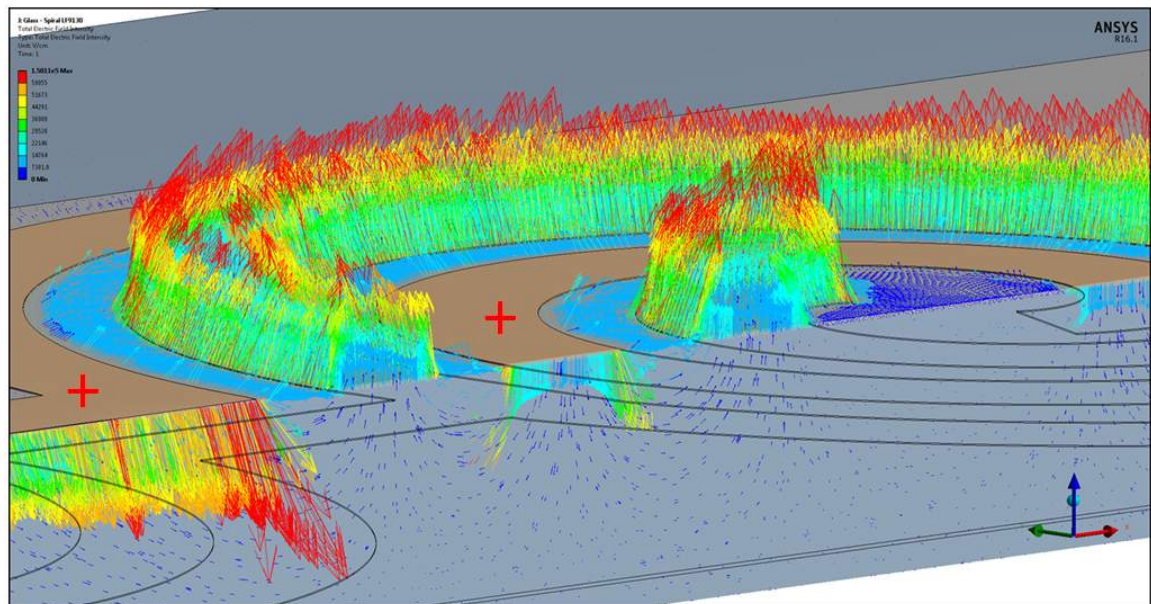


Figure 4.16. Close Up of Electric Field Vectors on the Insulator Surface

4.4.4 Four Tooth Pad Analysis

Figure 4.17 shows the voltage distribution of the four tooth assembly in contact with the aluminum body. Again, It is observed that since the adhering body is conductive, the highest voltage gradient exists between the positive electrode and the aluminum surface(ground).

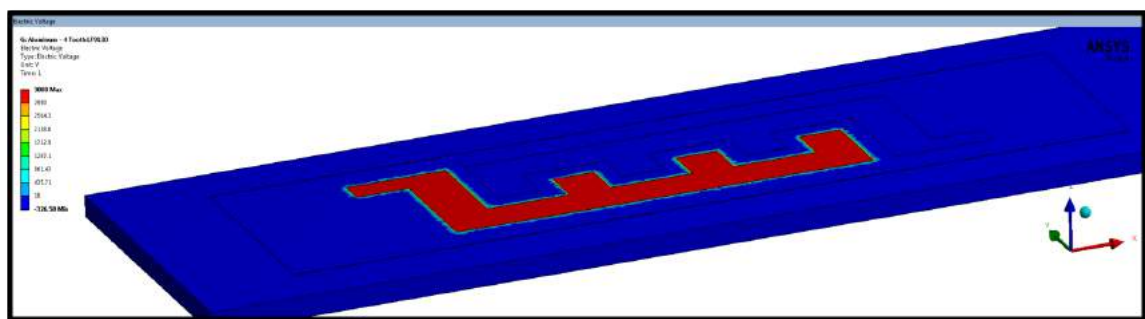


Figure 4.17. Voltage distribution for Conductive Surface

Figure 4.18 shows the electric field distribution. It is observed that the highest electric fields are occurring between the positive electrode and the aluminum surface. An average electric field of 34,175 V/cm is calculated between the electrodes.

Figure 4.19 shows a close up of the electric field vectors through the thickness of the assembly.

Figure 4.20 shows the voltage distribution assuming that the adhering surface is the glass body. It is observed that since the adhering body is an insulator, the voltage gradient is spread throughout the assembly.

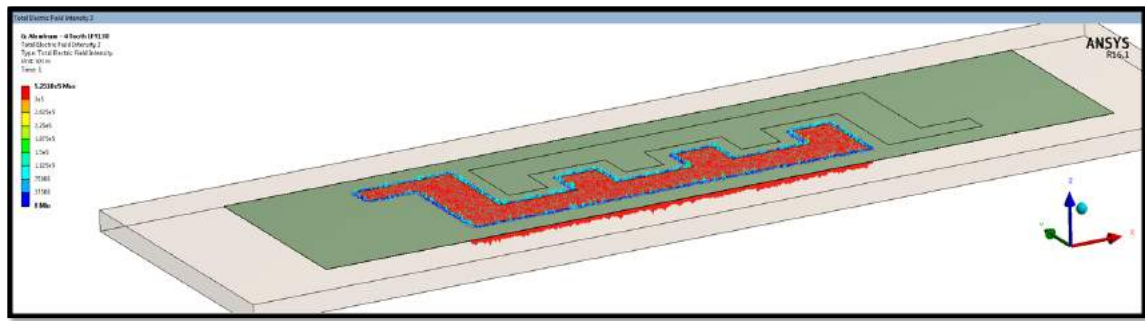


Figure 4.18. Electric Field Between Electrodes for Conductive Surface

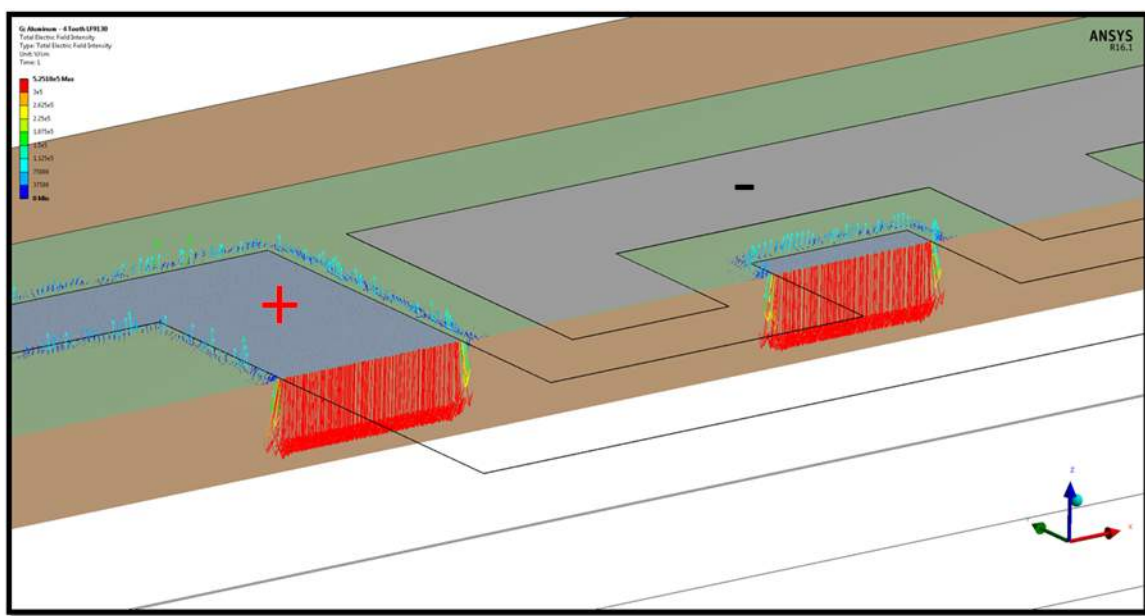


Figure 4.19. Close Up of Electric Field Vectors Under Conductive Surface

Figure 4.21 shows the electric field distribution with the glass surface. An average electric field of 7,406 V/cm is calculated between the electrodes. Figure 4.22 shows a close up of the electric field vectors through the thickness of the assembly. The field

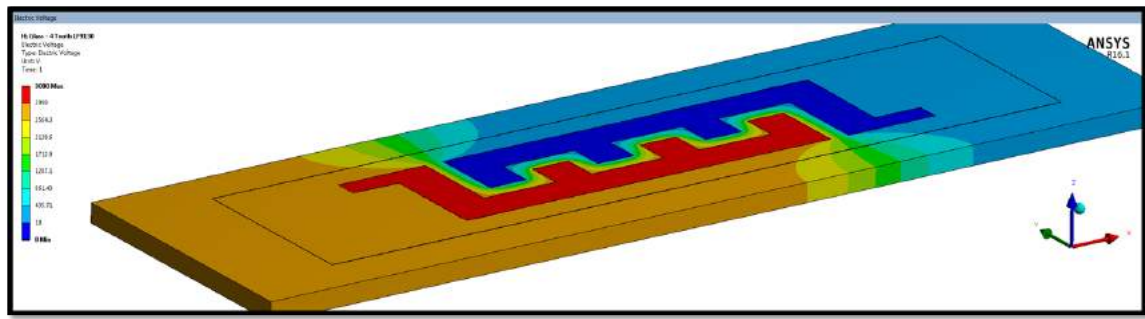


Figure 4.20. Voltage distribution for Insulator Surface

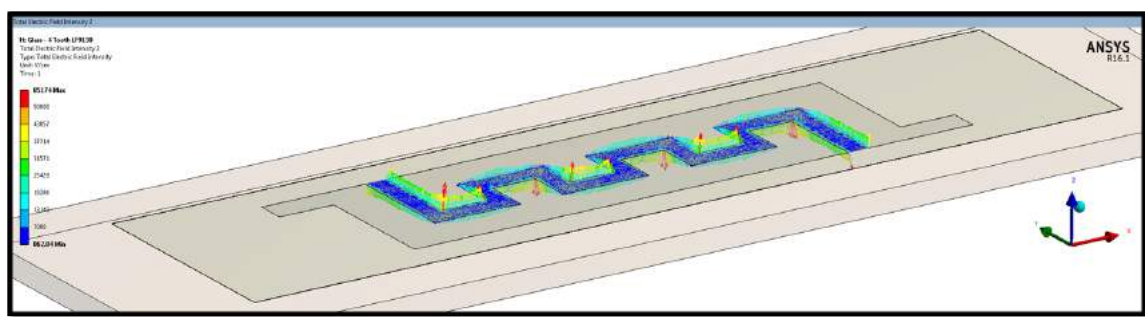


Figure 4.21. Electric Field Between Electrodes for Insulator Surface

vectors are also seen distributed from the positive to the negative electrodes using the glass surface as the medium of transportation.

4.4.5 Eight Tooth Pad Analysis

Figure 4.23 shows the voltage distribution of the eight tooth assembly with the conductive body. Again, It is observed that since the adhering body is conductive,

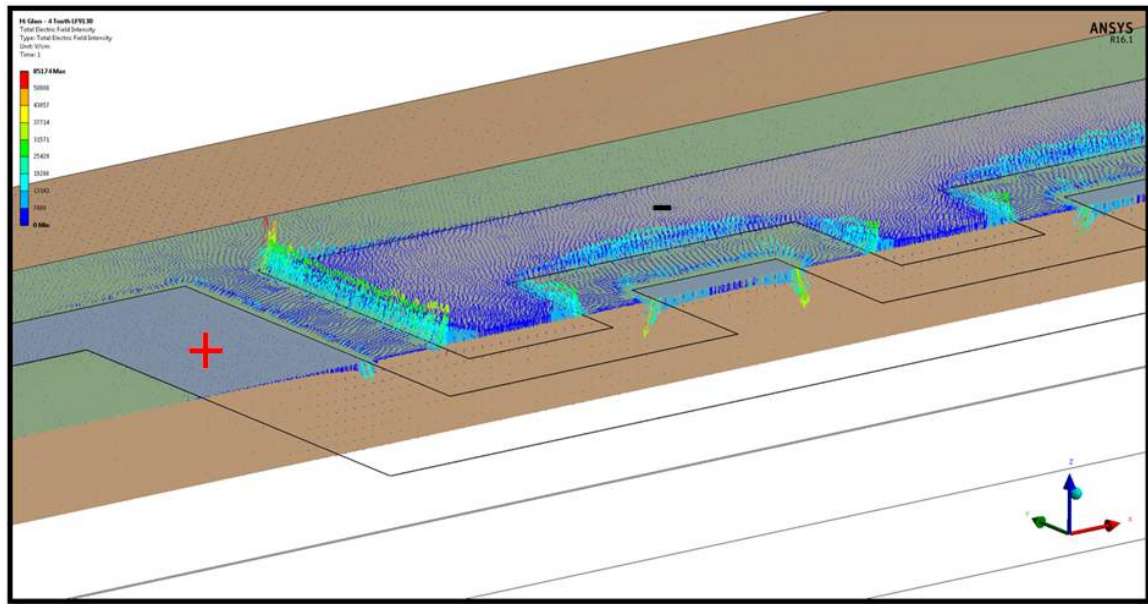


Figure 4.22. Close Up of Electric Field Vectors on the Insulator Surface

the highest voltage gradient exists between the positive electrode and the substrate surface (ground).

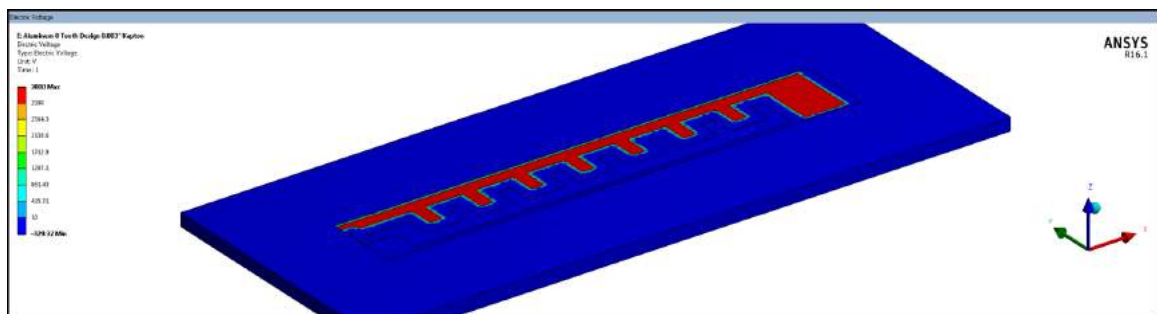


Figure 4.23. Voltage Distribution for Conductive Surface

Figure 4.24 shows the electric field distribution across the body. It is observed that the highest electric fields are occurring between the positive electrode and the aluminum surface. An average electric field of 33,237 V/cm is calculated.

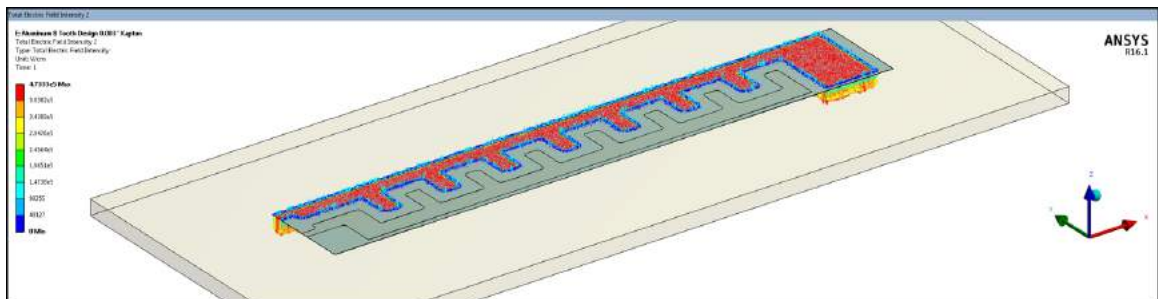


Figure 4.24. Electric Field Between Electrodes for Conductive Surface

Figure 4.25 shows a close up of the electric field vectors through the thickness of the assembly.

Figure 4.26 shows the voltage distribution assuming the adhering surface is glass. It is observed that since the adhering body is an insulator, the voltage gradient is spread throughout the assembly. Figure 4.27 shows the electric field distribution for the glass surface configuration. An average electric field of 6,890 V/cm is calculated between the electrodes. Figure 4.28 shows a close up cross sectional view of the electric field vectors through the thickness of the assembly. The field vectors are also seen distributed from the positive to the negative electrodes using the glass surface as the medium of transportation. It was observed that the electric fields on the eight tooth pad were very similar in magnitude and direction to those found in the four

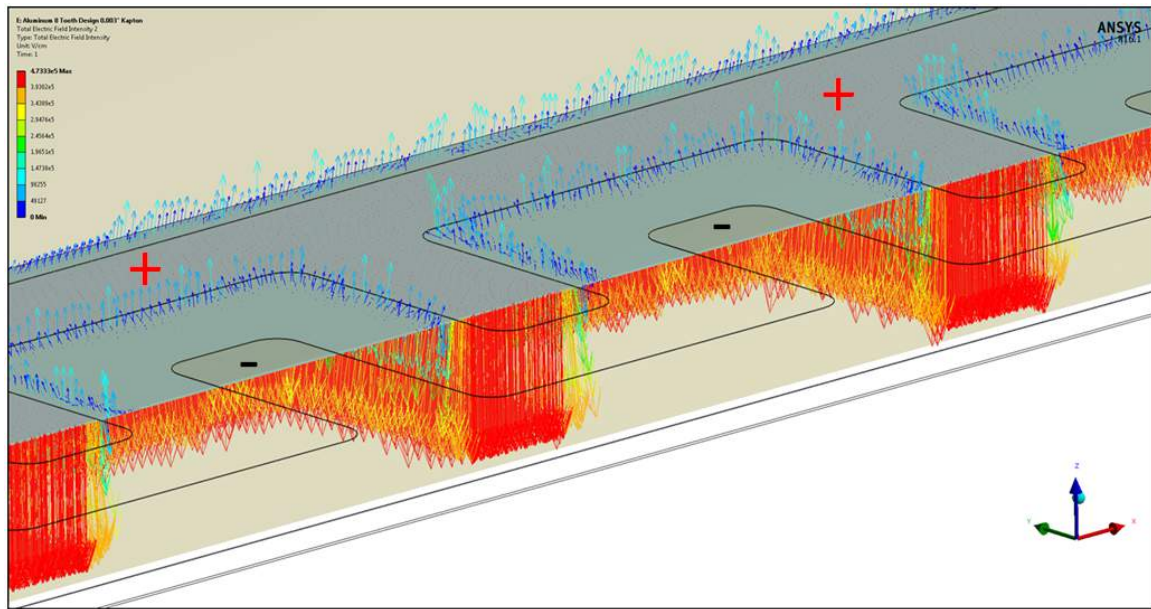


Figure 4.25. Close Up of Electric Field Vectors Under Conductive Surface

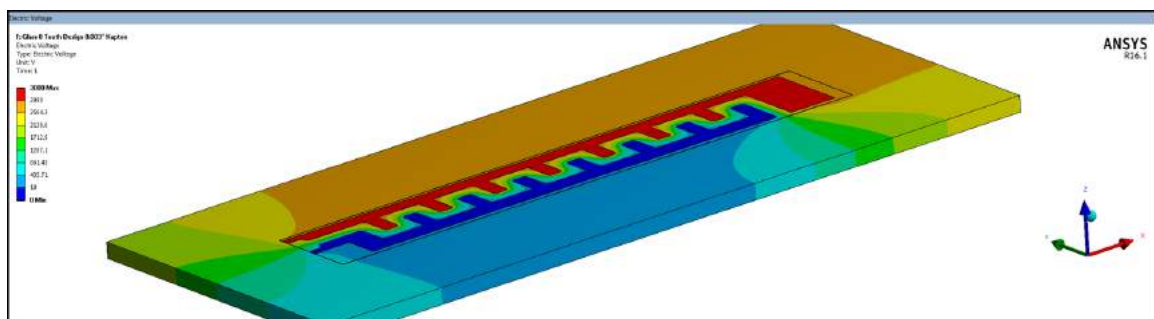


Figure 4.26. Voltage distribution for Insulator Surface

tooth pad. The arrows on the close up electric field views are scaled in color and in magnitude of value.

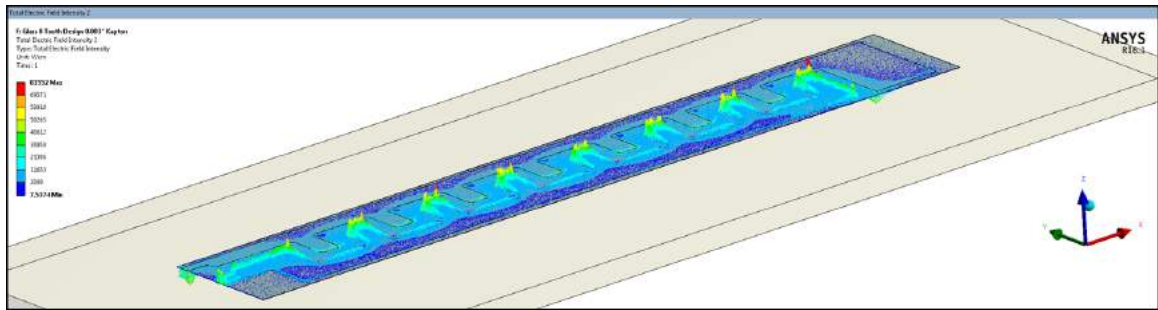


Figure 4.27. Electric Field Between Electrodes for Insulator Surface

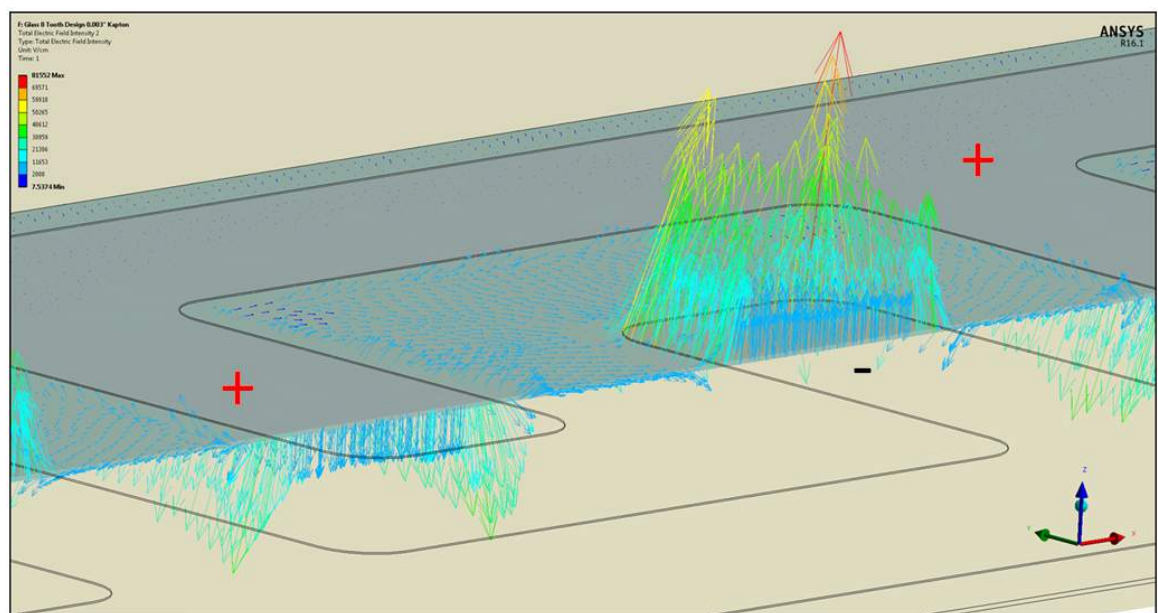


Figure 4.28. Close Up of Electric Field Vectors on the Insulator Surface

4.4.6 Summary of Finite Element Analysis Results

Based on the analyses performed in Section 4.4.1, it was confirmed that the electric field intensities increase as the electrode gap distance decreases. Based on the analyses

Table 4.3. FEA Results Comparison Between the 3 Main Pad Designs

Pad Design	Adhering Surface	Electrode Surface Area (cm²)	Average FEA Electric Field (V/cm)
Spiral	Metal	35.3	41,571
Four Tooth	Metal	33.7	34,175
Eight Tooth	Metal	29.6	33,237
Spiral	Glass	35.3	18,177
Four Tooth	Glass	33.7	7,406
Eight Tooth	Glass	29.6	6,890

performed in Section 4.4.2, it was calculated that minimal change in electric field intensity was present between a 0.005 cm and 0.0076 cm insulation thickness. Varying the thickness even further may have a more noticeable impact on the electric field.

Table 4.3 shows the comparison of average electric fields calculated in the FEA for the three main pad designs. A total of six cases were analyzed for the three pads. The table shows the pad design, the adhering surface type, the total electrode surface area, and the average electric field calculated. It was determined that the spiral design achieved the highest average electric field out of the three designs.

The four tooth and eight tooth pad designs resulted in a similar average electric field. The main variables that caused the electric field to be higher for the spiral design is the geometry of the electrodes and the electrode gap distance. It is also observed that the average electric fields were higher when adhering to a metal(conducting) surface. This is mostly due to the fact that a higher voltage gradient is present between the metal surface and the electroadhesion pad. The highest peak electric field

calculated out of the three models was 516,300 V/cm on the spiral design insulation when adhering to the conductor. Even with this high peak electric field, a minimum safety factor of 3.96 was achieved based on the 2,47,200 V/cm dielectric strength. Based on the electrostatic analysis, no dielectric breakdown is predicted on any of the analyzed pads when subjected to 3,000 V.

5. Fabrication of Electroadhesion Pads

5.1 Initial Fabrication Method

Initially, in order to have a proof of concept for the theory of electroadhesion, simple and easily obtainable materials were used in order to fabricate a pad. Easily obtainable materials such as aluminum foil, cellulose acetate (transparency film), and electrical tape were used.

Simple designs were sketched by hand and then traced onto an aluminum foil sheet. The traced designs were cut with scissors and then glued onto the acetate film with conductive adhesive gel. Once the adhesive was fully cured (left overnight to cure), a layer of 3M 33+ electrical tape was applied in order to prevent tracking between electrodes and also to eliminate the direct exposure of voltage while performing testing. Figure 5.1 shows one of the pads that was fabricated for proof of concept. It is comprised of a U-shape design with an electrode gap of 1 cm.

The concept using the initial fabrication method resulted in 1 N of average adhesion force when tested on a glass surface, which proved the concept of electroadhesion before moving on to more sophisticated and complex pad designs. One disadvantage of the initial fabricated pads is that they required large amounts of time in order to trace and cut the designs precisely. The limitations of the pad are that since the electrodes were manually cut and adhered, it was difficult to create any complex design.

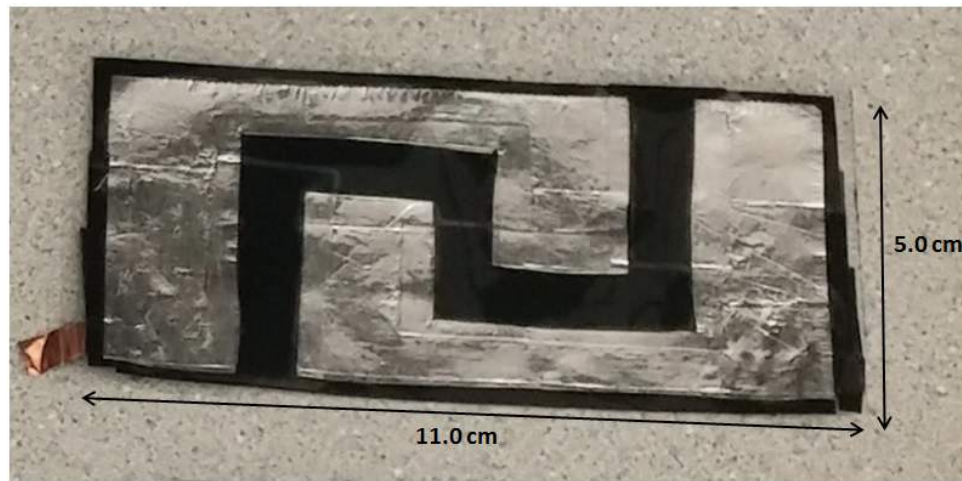


Figure 5.1. Initial "U-Shape" Proof of Concept Pad

Additionally, the gap distances between electrodes could not be reduced easily due to potential tracking caused by the conductive adhesive.

5.2 Fabrication Using Etching

A more elaborate method of fabricating the electroadhesion pad was employed by using a flexible copper clad composite and chemically etching the electrode designs. The material of choice for the electroadhesion pads consisted of Dupont Pyralux LF9130, which is a composite three layer laminate consisting of polyimide film, adhesive, and copper. The sheets were obtained directly from Dupont and are available in various sizes and configurations. The LF9130 sheet used is approximately 0.0126 cm thick. Figure 5.2 shows a cross section of the layers within the LF9130 composite along with the nominal dimensions.

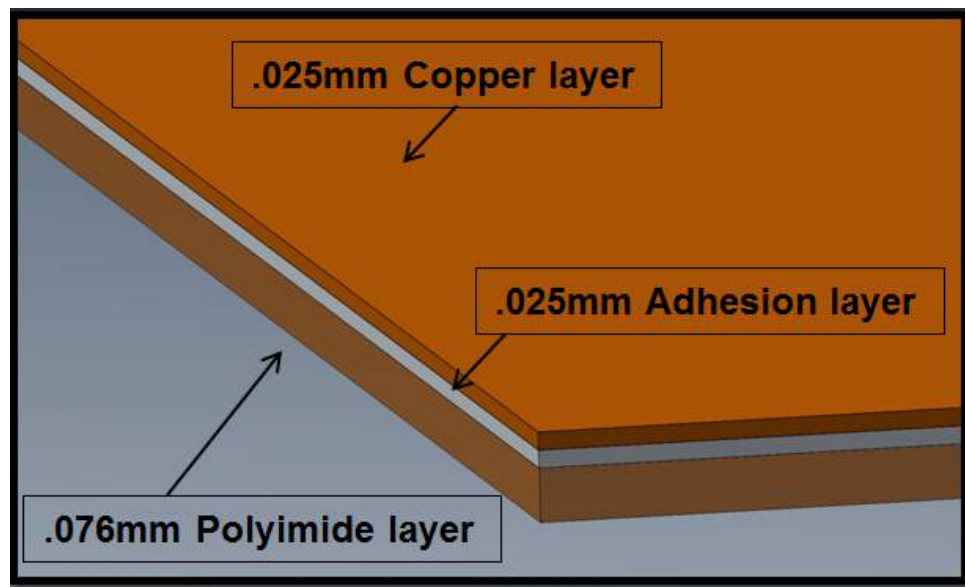


Figure 5.2. Cross Sectional Illustration of LF9130

The electrode designs were designed using CAD software as discussed in chapter 3. Then, the designs were printed onto the Pyralux sheets using a Xerox ColorQube solid ink printer. Solid ink printers use melted wax instead of liquid ink as found in more common inkjet or powder as in laser printers. It was necessary to use wax instead of ink due to the fact that the wax adheres to the copper, which allows printing of complex, fine-detailed designs. The solid ink printer essentially heats up the solid colored wax until they are in liquid state and then prints onto the sheets (Kazmeyer, 2007). Once the designs were printed onto the Pyralux sheet, they were immediately placed into a refrigerator for at least 10 minutes in order to fully cool down and solidify the wax. Placing the sheets in the refrigerator helps cool down the copper, since some heat is transferred to the copper layer during the printing process.



Figure 5.3. Printed Designs on Pyralux sheet

At this point, the pad consists of four layers; polyimide, adhesive, copper, and solid wax (printed design). Figure 5.3 shows an example of printed designs on the Pyralux sheet. In order to create the printed electrode design as the copper layer, it was necessary to etch away the remaining copper that was not covered with wax. Ferric chloride was used in order to etch the copper until all that remained was the polyimide sheet along with the copper electrode designs. The etching process using ferric chloride is a common method of etching designs on copper clads and is also used to fabricate circuit boards. This method was used due to the fact that the ferric chloride is easily obtainable and it does not produce dangerous fumes, it is not absorbed through the skin, and it is odorless. Refer to Appendix X for the safety procedures used for the etching process.

The printed Pyralux is submerged in a tub of ferric chloride until the undesired copper layer is etched away (typically takes 30-45 minutes per pad). Figure 5.4 shows

a picture of the Pyralux sheet with printed designs submerged in a bath of ferric chloride.



Figure 5.4. Pyralux Pads Submerged in Ferric Chloride

Once the etching process is complete, the pad is rinsed in water to remove any excess ferric chloride solution. Figure 5.5 shows the pads once they have been etched and rinsed in water. The electrode designs are still covered in the wax layer that protected it from being etched away.

Since the printed wax layer was used to protect the surface of the electrode copper from etching, the remaining wax layer was removed by scrubbing the pad with acetone and a rough scrub. Figure 5.6 shows a completely etched pad. Now the pad consists of three layers again, but now with the copper layer as the electrode shape only.

Once the pad is etched, a layer of 3M electrical tape is applied on the exposed electrode side in order to prevent tracking and to prevent shocking to the person performing electrical experiments. Figure 5.7 shows an image of the spiral electrode-



Figure 5.5. Etched Pads With Remaining Wax Layer



Figure 5.6. Completely Etched Pads with Exposed Electrode Designs

hesion pad with the electrical tape layer applied. Next to the electroadhesion pad is the MFC that is used as an actuator.



Figure 5.7. Spiral Pad with Insulation Tape

The MFC actuator is attached to the electroadhesion pad by taping it using a 0.0076 cm thick polyimide tape. Figure 5.8 shows the final electroadhesion pad assembly including the attached MFC actuator.



Figure 5.8. Spiral Pad with attached MFC actuator

6. Experimental Verification

6.1 Test Purpose

Experiments were performed on the finalized pads that were analyzed and fabricated in order to determine the shear adhesion capabilities. The main pad designs that were chosen to test extensively were the spiral, four tooth, and eight tooth designs. A comparison of average shear adhesion was desired for the main pad designs. Experiments were also performed in order to determine the correlation between electric field and the adhesion force. All experiments were performed at room temperature conditions in air. In reality, the electroadhesion pads will have to function in a vacuum environment in space. Studies have been performed by NASA and SRI International on the effects of electroadhesion pads in vacuum (Pelrine, 2009), but cannot be replicated at the time of this thesis due to lack of vacuum facility. Figure 6.1 shows that pads tested under a vacuum resulted in higher adhesion force for multiple substrate thicknesses. The dimensions or shapes for the electroadhesion pads that NASA and SRI used were not disclosed, but based on the graph, it is clear that adhesion levels should be higher under a vacuum environment. This is most likely due to the absence of air trapped between the electroadhesion mechanism and adhering body. It also seems that the effect of the vacuum environment increases the adhesion as the substrate thickness decreases. Again, this is most likely due to the absence of

air as there is a higher probability of having larger air pockets as the thickness of the insulation increases.

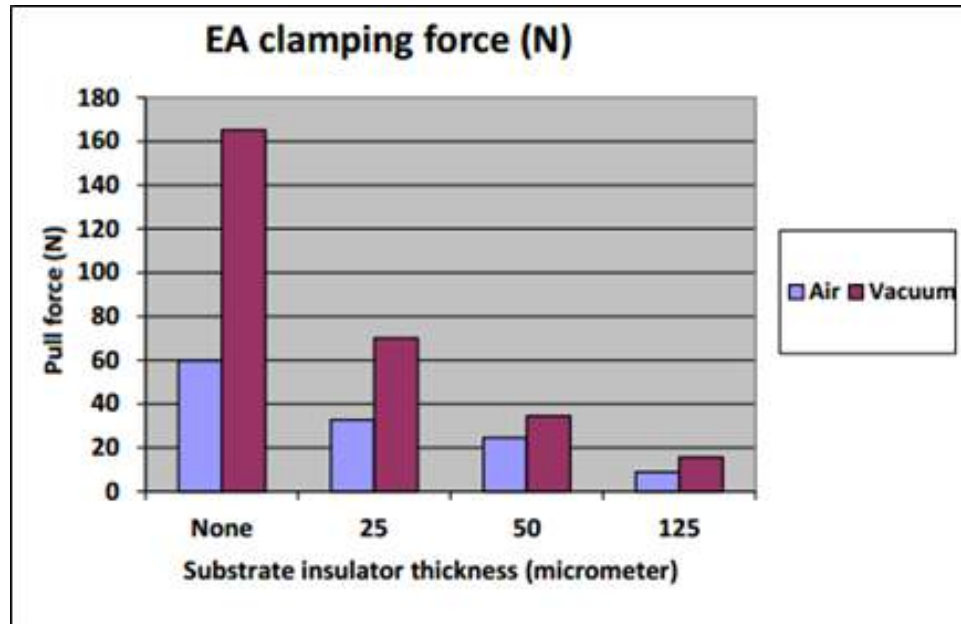


Figure 6.1. Tested Pads in Air and Vacuum (Pelrine, 2009)

6.2 Experimental Design

6.2.1 Materials and Equipment Used

In order to verify the electroadhesion capabilities of the designed pads, it was necessary to apply a voltage gradient by connecting the pad terminals to a high voltage power supply. A Glassman MJ3P5000 3,000 V power supply was used. The power supply runs with a maximum current of 5 mA, which gives a total power of 15 W. Figure 6.2 shows an image of the Glassman high voltage power supply used for testing of the electroadhesion pads.



Figure 6.2. Glassman MJ3P5000 3kV Power Supply

An electrical insulator and a conductor body was used in order to test the pads. Figure 6.3 shows a curved aluminum T6-6061 panel, which has a curvature radius of 0.6 m. Figure 6.4 shows a glass surface that was used for experimentation on an insulator body. The glass surface is much smoother than the aluminum surface on the conductor body used. In order to record the peak shear adhesion generated by each pad, a Shimpo FGV series force gage was used to manually pull and record each test. Figure 6.5 shows the digital force gage (Shimpo FGV) used in order to record the



Figure 6.3. Aluminum Surface used for Testing

peak adhesion force generated from the tested pads. The force gage was connected to a PC during testing in order to plot the force vs. time on every pull test performed.

The equipment described above was used to test the shear adhesion of the three pads tested. Out of the three pads, the one with the highest average adhesion force was selected to test with the MFC actuator. In order to actuate the MFC, a separate power supply was needed to provide the 0 to 1,500 V. A 12 V power supply was used in conjunction with an AMT2012-CE3 (figure 6.6) dual high voltage amplifier that converts 0 to 5 Volts into -500 to +1,500 Volts. The actuator's deflection is dependent on the applied voltage, therefore in order to control the magnitude and frequency of

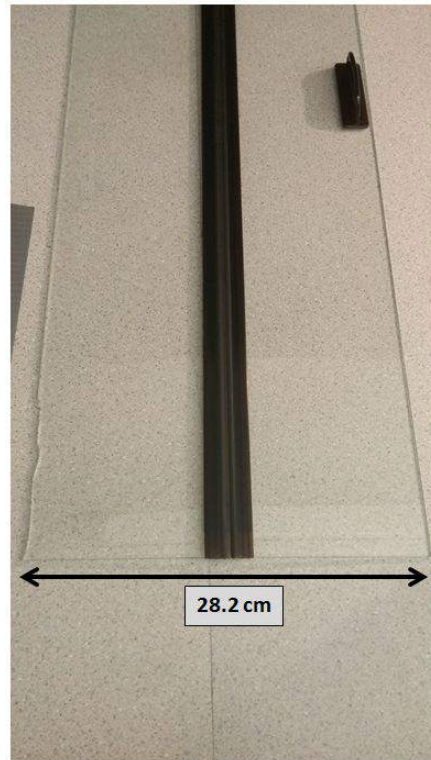


Figure 6.4. Glass surface used for Testing



Figure 6.5. Shimpo FGV Series Force Gage



Figure 6.6. AMT2012-CE3 Amplifier



Figure 6.7. myDAQ DAQ System

the signal, a National Instruments myDAQ(figure 6.7) was used in conjunction with LabVIEW .

6.2.2 Test Setup

All tests were performed with safety precautions due to the fact that high voltage was present. Although low current of 5 mA was used, it was still possible to get shocked if not wearing the proper protective equipment. Refer to appendix D for the safety guidelines on performing high voltage tests for this thesis.

Figure 6.8 shows an image of the test setup used for the aluminum body. The spiral electroadhesion pad is shown being tested without the use of the MFC actuator.



Figure 6.8. Test Setup on Aluminum Surface

The purpose of this test was to determine adhesion of the pad itself with no actuation. The electroadhesion pad was energized by activating the 3kV power supply and the pad was layed on the surface of the adhering body until ready to start the shear pull tests. The same test procedure was used for testing the glass body. It is important to note that the force gage was pulled manually in order to record the shear peak during every pull test conducted. Figure 6.9 shows a schematic of the hardware setup used for supplying power to the electroadhesion pad and the attached MFC. The DAQ system was connected to a PC, the power supply, and the amplifier. LabVIEW software was used to control the input voltage and frequency on the amplifier which was feeding into the MFC actuator.

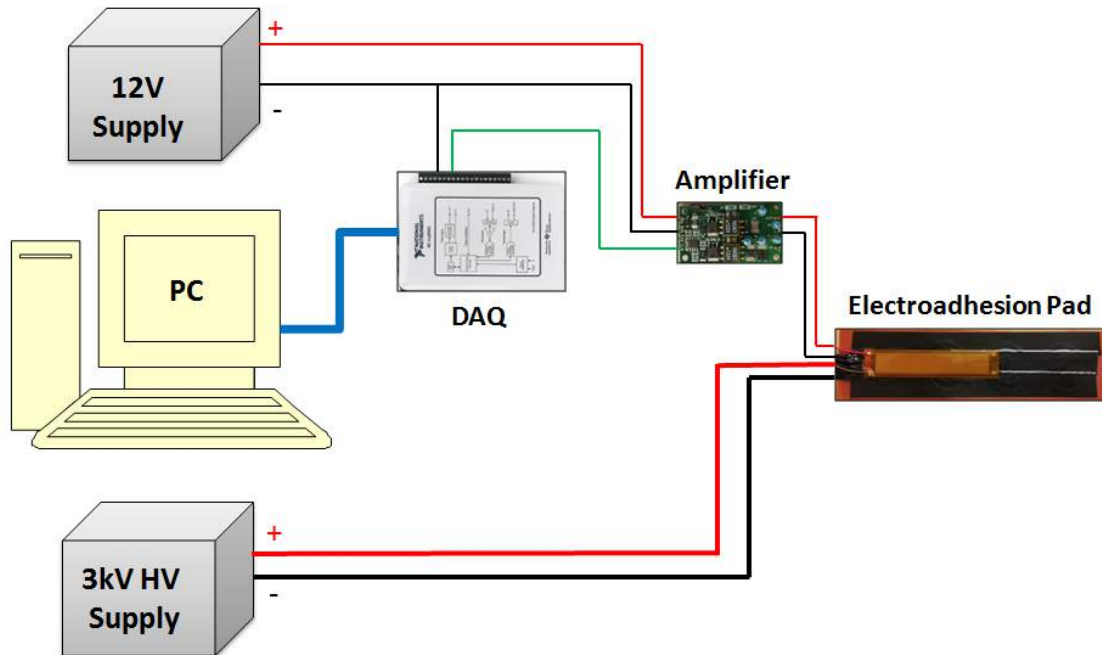


Figure 6.9. Schematic of Hardware Setup for MFC and Electroadhesion Pad

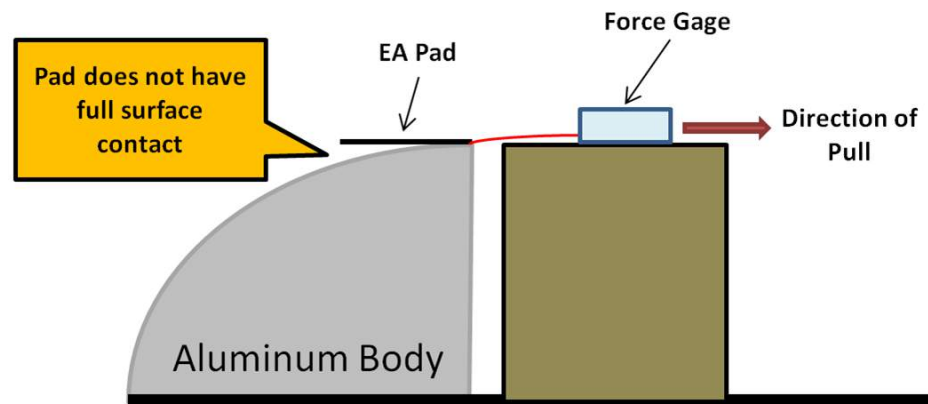


Figure 6.10. Schematic of Test Setup for MFC Actuation

One of the drawbacks of the electroadhesion pad is that the adhesion is a function of the surface contact attained during docking. When encountering a surface with

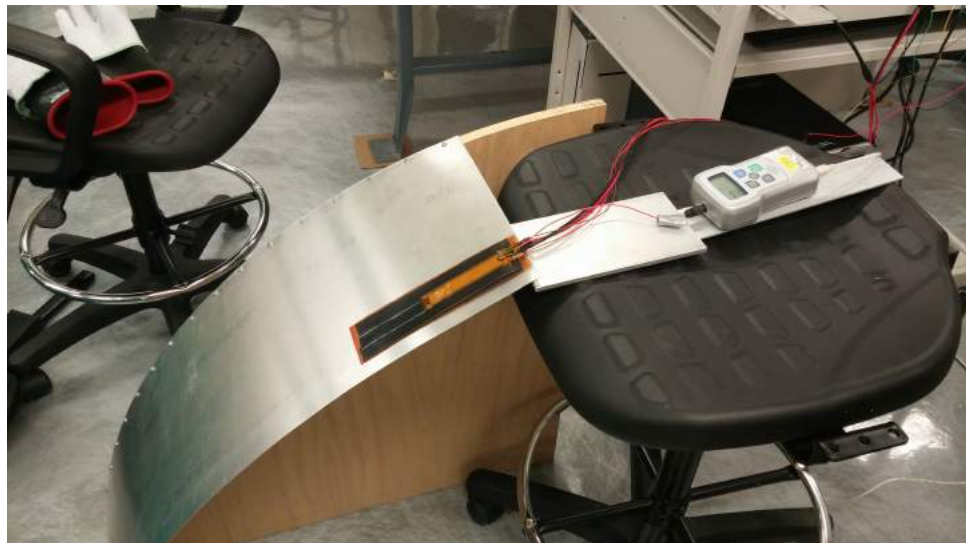


Figure 6.11. Test Setup to Determine Adhesion with MFC Use

curvature, this may present some difficulty in attaining as much contact as possible, which is why actuators were used. Figure 6.10 shows a schematic of the test setup used to test the adhesion with the use of an actuated MFC. The pad was placed at the edge of the quarter circle aluminum body in a tangential positions where only 50-60% of the pad is in contact with the aluminum surface. A set of tests were performed to measure the average adhesion without any actuation and then the MFC was actuated in order to remeasure adhesion. Figure 6.11 shows the image of the actual test setup used to compare the adhesion with and without the use of MFC actuation.

6.3 Results

6.3.1 Electroadhesion Results

Figure 6.12 shows the graph of the shear adhesion vs time when testing the spiral pad on the curved aluminum substrate with no MFC actuated. A total of 16 tests were performed per test configuration. A peak adhesion force of 3.1 N was achieved. As observed in the graph, once the peak adhesion is obtained, further pulling detaches the pad from the substrate and starts to slide along the surface. The test is stopped once the pad loses adhesion force.

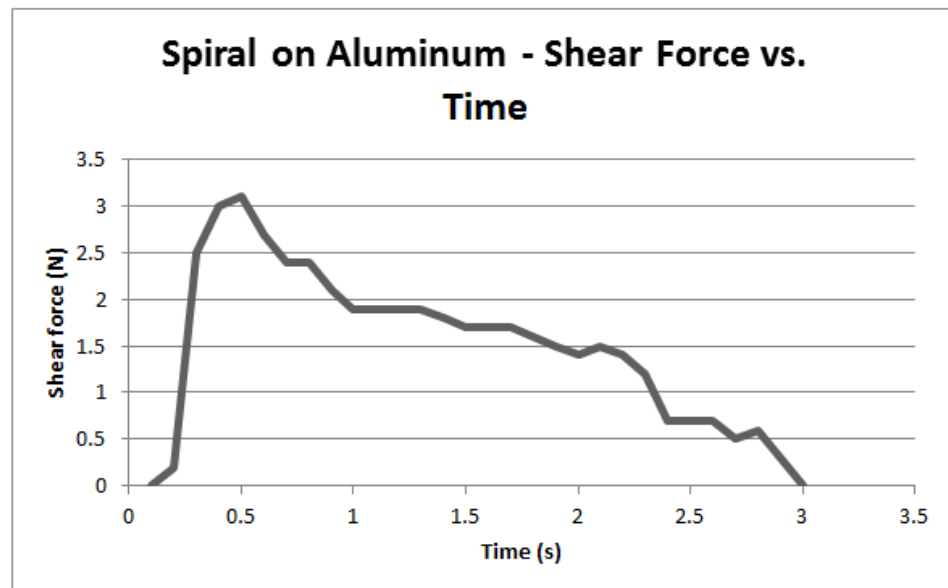


Figure 6.12. Peak Adhesion with Spiral Pad on Aluminum

Figure 6.13 shows a similar graph, but when testing the spiral pad on the glass substrate. A peak adhesion force of 11.3 N was achieved. The generated adhesion of the spiral pad on the glass substrate is much higher than on the aluminum substrate.

Based on the electric field analyses described in Chapter 4, electric fields were much higher on the conductive configuration than the insulator configuration. Theoretically, it was expected to achieve higher adhesion on the conductor configuration, but the main reason for this difference is that the glass surface is much smoother than the aluminum surface. A better contact is achieved between the pad and the smooth glass, hence adhesion levels are higher.

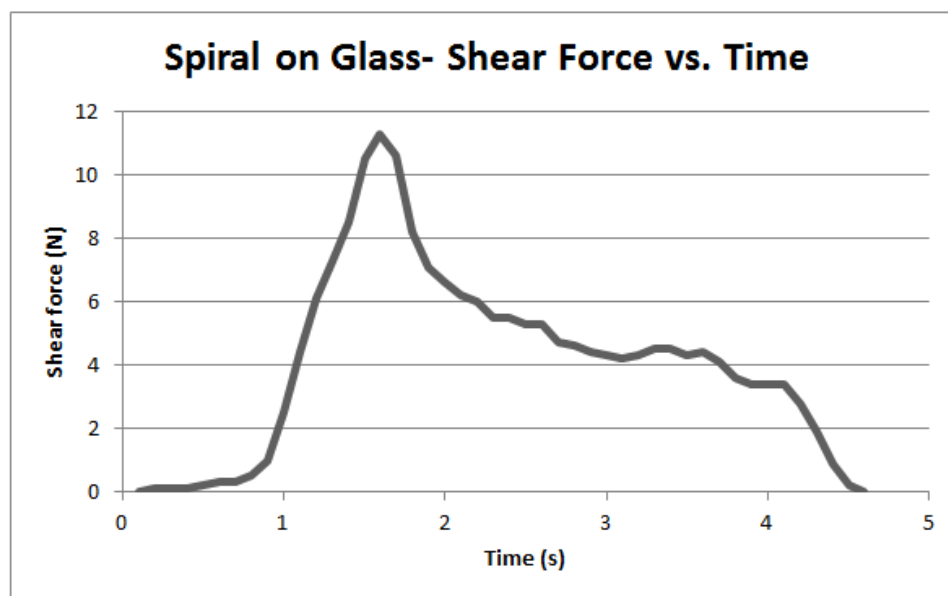


Figure 6.13. Peak Adhesion with Spiral Pad on Glass

Figure 6.14 shows the graph of the shear adhesion vs. time when testing the four tooth comb pad on the curved aluminum substrate. A peak adhesion force of 2.2 N was achieved.

Figure 6.15 shows a similar graph, but instead testing the four tooth pad on the glass substrate. A peak adhesion of 5.4 N was achieved. Again, higher adhesion force

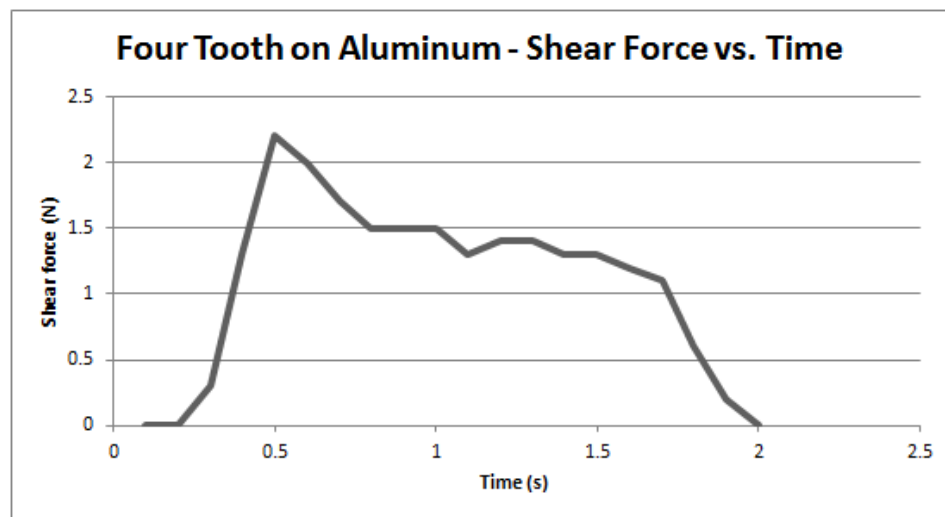


Figure 6.14. Peak Adhesion with Four Tooth Pad on Aluminum

was achieved on the smooth glass substrate due to the better contact obtained during testing.

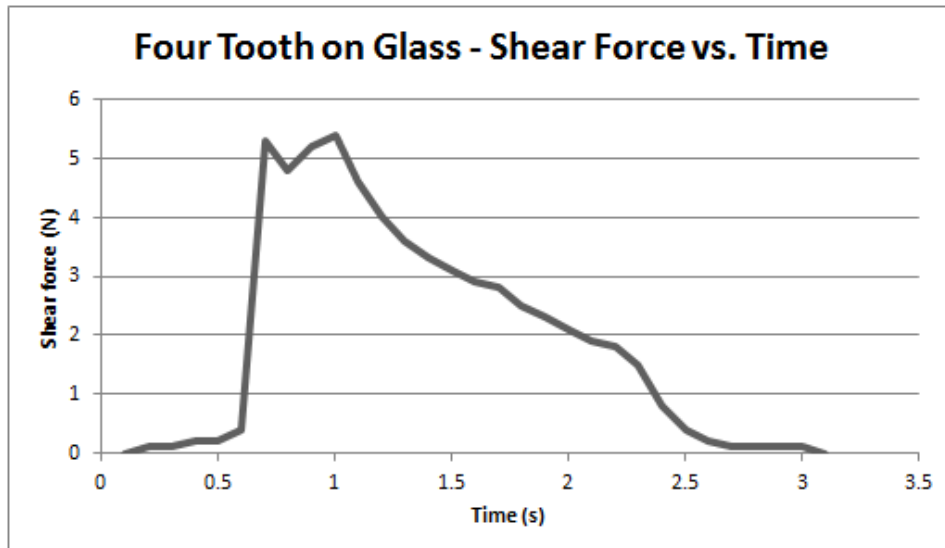


Figure 6.15. Peak Adhesion with Four Tooth Pad on Glass

Figure 6.16 shows the graph of the shear adhesion vs. time when testing the eight tooth comb pad on the curved aluminum substrate. A peak adhesion force of 2.4 N was achieved.

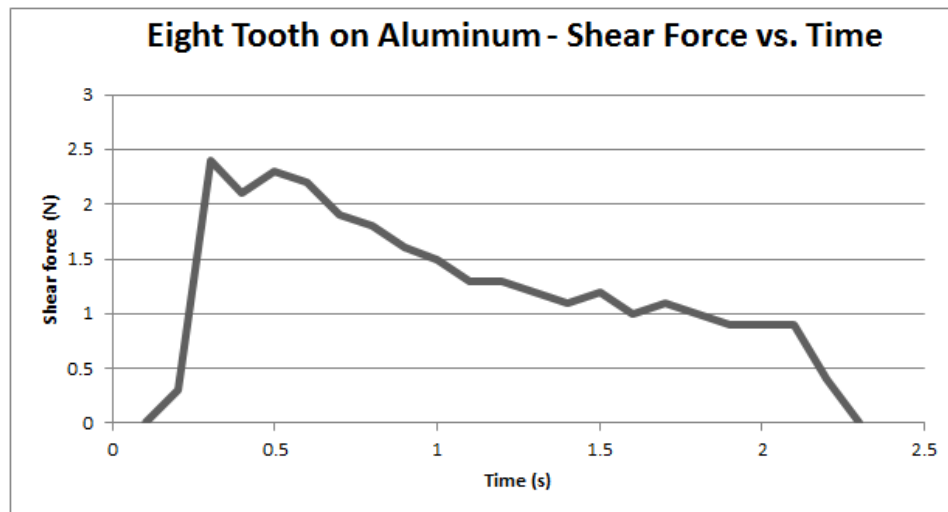


Figure 6.16. Peak Adhesion with Eight Tooth Pad on Aluminum

Figure 6.17 shows a similar graph, but instead when testing on the glass substrate. A peak adhesion of 6.1 N was achieved. Higher adhesion force is also achieved on the smooth glass substrate due to the better surface contact obtained during testing.

In order to compare the performance of the three pad configurations tested, a graph was created showing the average adhesion force from each pad when adhering to the aluminum surface (Figure 6.18). A total of 16 manual pull tests were performed per pad configuration. The average adhesion was 2.91 N for the spiral pad, 1.93 N for the four tooth pad, and 2.07 N for the eight tooth pad design. The standard deviations calculated for the spiral, four tooth, and eight tooth pads were 0.15 N, 0.17 N, and 0.16 N, respectively. Based on the graph results, it is noticeable that the

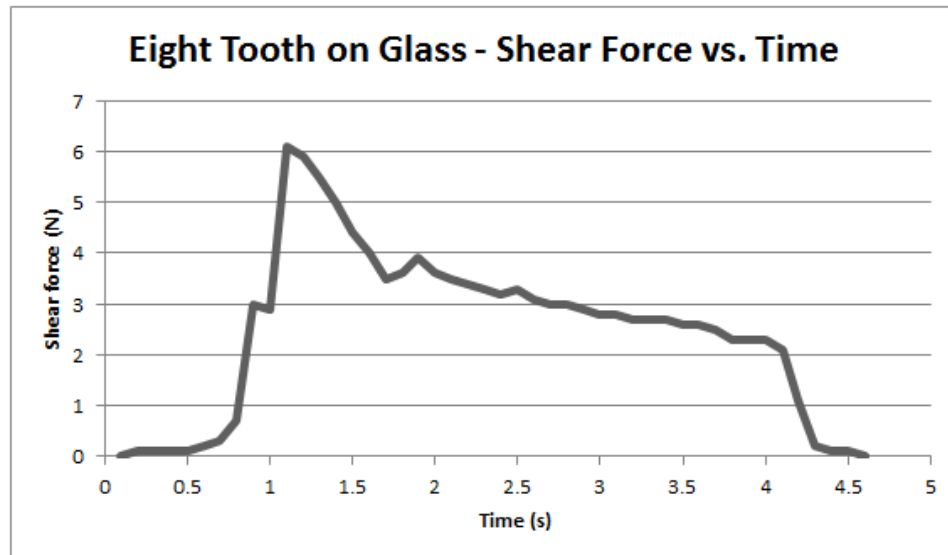


Figure 6.17. Peak Adhesion with Eight Tooth Pad on Glass

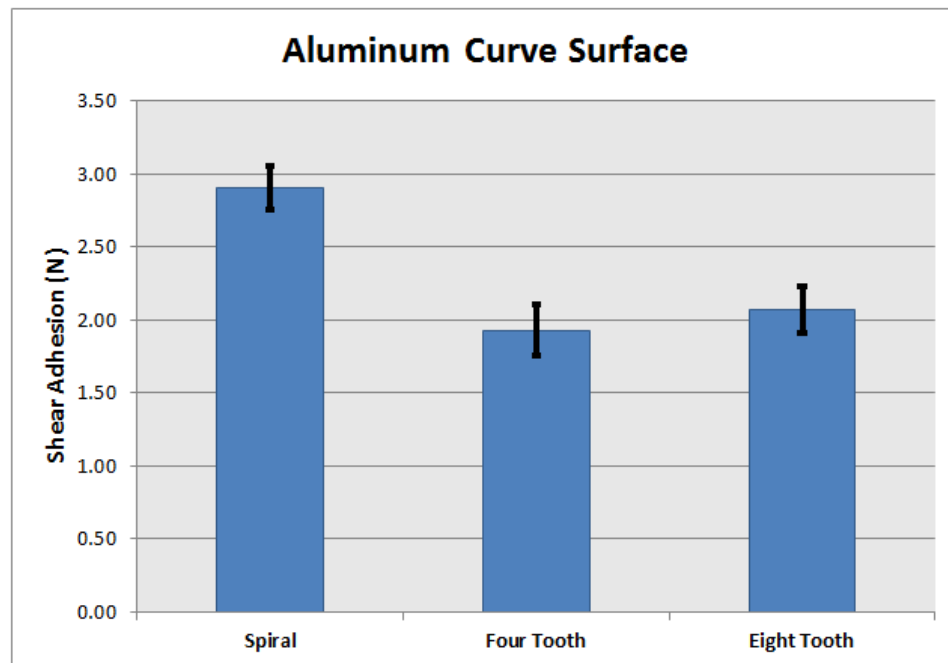


Figure 6.18. Average Adhesion of Pads on Aluminum

Table 6.1. Standard Deviation Values for Test Results

Pad Design	Adhering Surface	Standard Deviation (N)
Spiral	Metal	0.15
Four Tooth	Metal	0.17
Eight Tooth	Metal	0.16
Spiral	Glass	0.50
Four Tooth	Glass	0.20
Eight Tooth	Glass	0.20

spiral resulted in the highest average adhesion force out of the three pad configurations when testing on the conductive surface. Figure 6.19 shows a graph of the average adhesion force from each pad when adhering to the glass surface. Again, a total of 16 manual pull tests were performed per pad configuration. The average adhesion was 10.28 N for the spiral pad , 5.09 N for the four tooth pad, and 5.73 N for the eight tooth pad design.

The results of the tests are tabulated in Table 6.2. The standard deviations for the spiral, four tooth, and eight tooth pads are 0.50 N, 0.2 N, and 0.2 N, respectively (shown in Table 6.1). Based on the graph results, it is noticeable that the spiral resulted in the highest average adhesion force out of the three pad configurations when testing on the insulator surface.

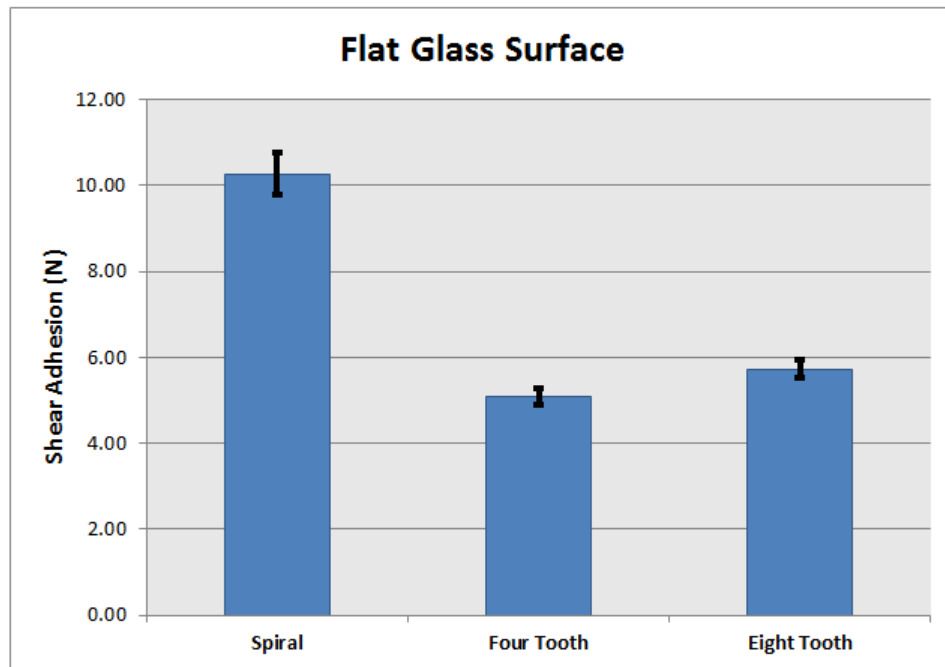


Figure 6.19. Average Adhesion of Pads on Glass

6.3.2 Results of Electroadhesion Using MFC

Figure 6.20 shows the graph of the shear adhesion vs. time for the electroadhesion pad tested at a tangential position on the curved aluminum (setup in figure 6.10) without MFC actuation. A peak shear adhesion of 0.9 N was achieved for this configuration. The same test was completed but with the use of the MFC actuator. Maximum voltage of 1,500 V was supplied to the MFC in order to provide full actuation. Once the MFC was actuated, it was observed that the electroadhesion pad had broader surface contact on the curvature. Figure 6.21 shows the peak adhesion obtained with the use of the MFC, which was 1.7 N. The peak adhesion with the use

of the MFC was almost double due to the added surface contact between the pad and the aluminum surface.

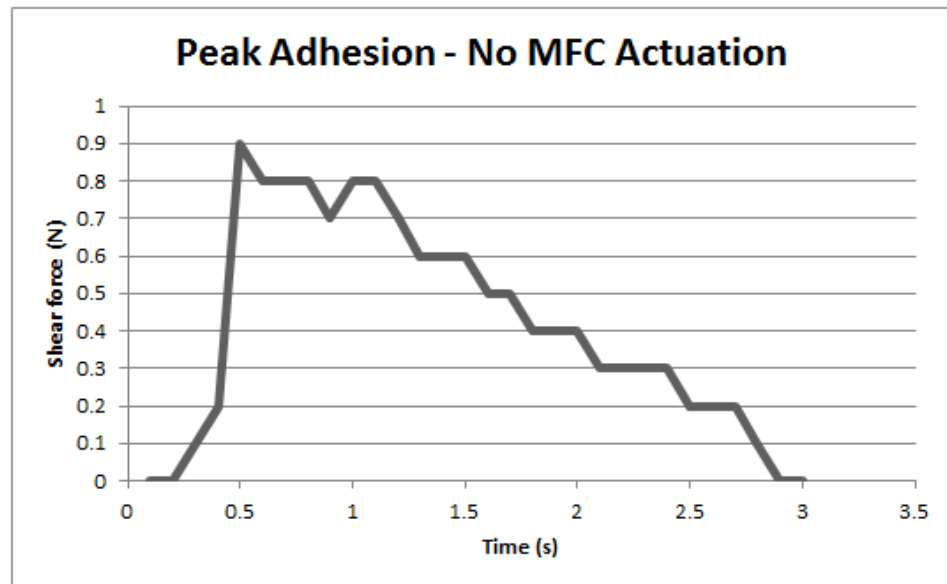


Figure 6.20. Peak Spiral Adhesion Without MFC Actuation

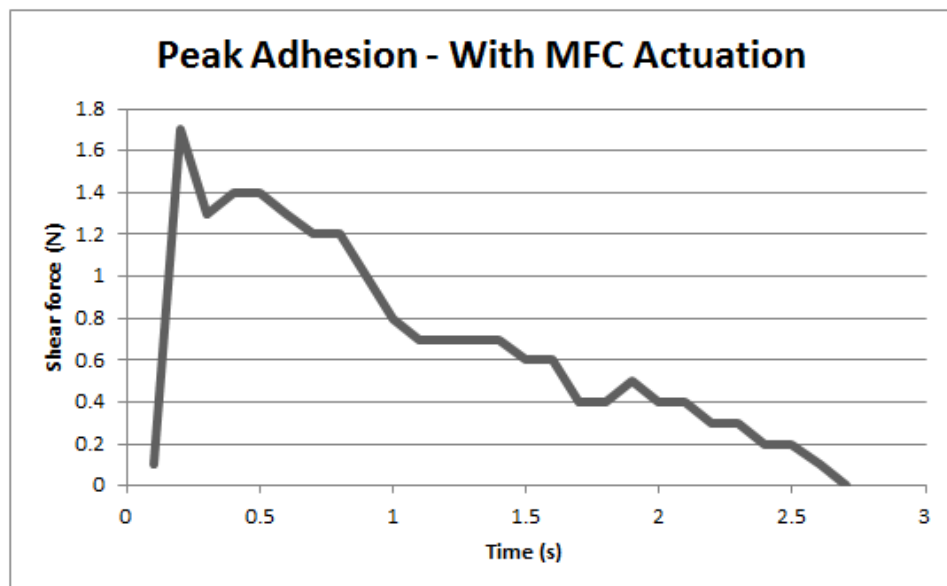


Figure 6.21. Peak Spiral Adhesion With MFC Actuation

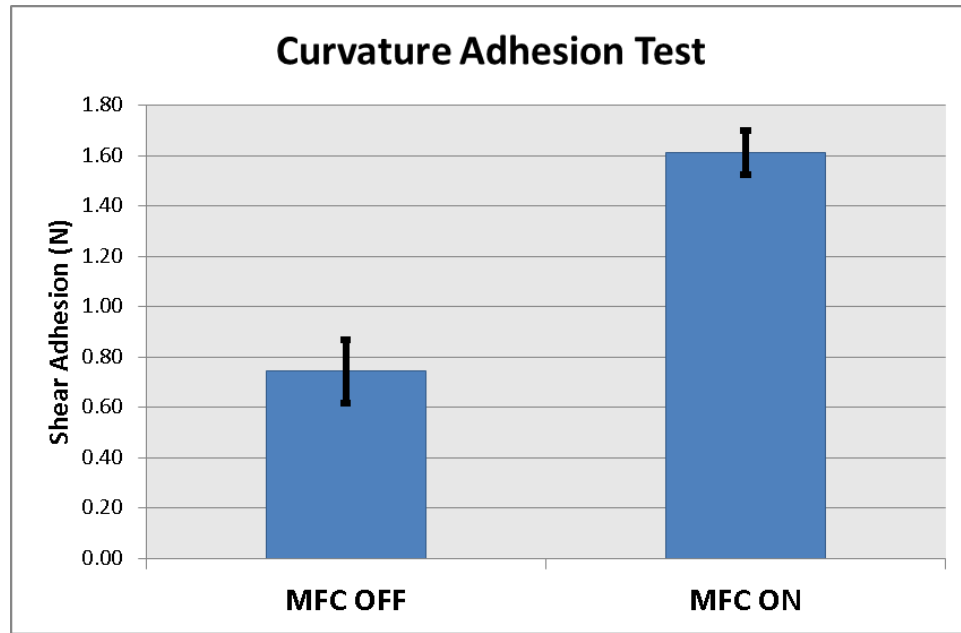


Figure 6.22. Average Adhesion of Spiral Pad With MFC Off and MFC On

A total of 16 manual pull tests were performed per test configuration. Figure 6.22 shows the comparison of average adhesion obtained with and without the use of the actuated MFC on the edge of the aluminum body. An average adhesion force of 0.74 N was obtained without the use of the actuated MFC. An average adhesion force of 1.61 N was obtained when actuating the MFC in order to obtain higher surface contact area. It is observed that the average adhesion is over twice as high when actuating the MFC.

6.4 Comparison with Theoretical Results

Based on the electrostatic finite element analyses performed in chapter 4, it was determined that the highest electric fields were calculated on the spiral pad design.

Table 6.2. FEA and Experimental Results Between the 3 Main Pad Designs

Pad Design	Adhering Surface	Electrode Surface Area (cm²)	Average FEA Electric Field (V/cm)	Average Shear Adhesion (N)
Spiral	Metal	35.3	41,571	2.91
Four Tooth	Metal	33.7	34,175	1.93
Eight Tooth	Metal	29.6	33,237	2.07
Spiral	Glass	35.3	18,177	10.28
Four Tooth	Glass	33.7	7,406	5.09
Eight Tooth	Glass	29.6	6,890	5.73

Hence, it was expected to achieve higher shear adhesion on the spiral design during testing. Table 6.2 shows the comparison of average electric fields calculated in the FEA along with the average adhesion obtained from testing. A total of six cases were performed for the three pads. The table shows the pad design, the adhering surface type, the total electrode surface area, the average electric field calculated, and the average shear adhesion. It was determined that the spiral design achieved the highest average electric field out of the three designs and also resulted in the highest adhesion force. The four tooth and eight tooth pad designs resulted in a similar average electric field and also similar adhesion forces. Based on the FEA, it was expected that the adhesion levels on the conductive body would be much higher than in the glass body configuration. Experimental tests showed that the glass resulted in much higher average adhesion force, which is mainly due to the fact that the glass body was far smoother than the surface on the aluminum body.

7. Conclusions and Future Work

7.1 Conclusion

The purpose of this research was to design an electroadhesion pad concept in order to be able to integrate in an orbital debris retrieval system. The pads were designed with the goal of being able to adhere to a wide variety of surface materials and curvatures. It was proposed to use an MFC actuator that would bend the electroadhesion pad when required to adhere to surfaces with curvature, since the amount of adhesion obtained is dependent on the amount of surface contact achieved.

Three pad geometries were analyzed in ANSYS using electrostatic finite element analysis to determine the electric fields between the different designs. A spiral, four tooth, and eight tooth design was analyzed when being subjected to a 3,000 V gradient between electrodes. Each pad was analyzed assuming the adhering body was either a conductor or an insulator. The highest average electric field was calculated on the spiral pad design for both adhering body configurations. The electric fields calculated between the four tooth and eight tooth pads were similar.

A fabrication technique involving the use of chemical etching on a copper clad composite was executed and successfully utilized to create three pad geometries for testing. This fabrication technique was crucial for being able to design and test the use of electroadhesion pads with complex electrode shapes.

Experimental tests were performed to determine the average adhesion force of the pads on the aluminum body and on the glass body. Results showed that the spiral design achieved the highest adhesion out of all pads with an average of 2.91 N on the aluminum surface and an average of 10.28 N on the glass body. The MFC actuator was attached to the spiral pad in order to test the adhesion of the pad with and without actuation on a surface with curvature. Without the use of actuation, the spiral was able to obtain an average adhesion of 0.74 N on the edge of a curved aluminum body. The MFC was then energized in order to actuate the pad and obtain higher surface area contact, which resulted in an average adhesion of 1.61 N. It is concluded that the spiral design resulted in the highest electric field and also the highest average adhesion forces during testing. The use of an MFC actuator in order to obtain higher surface contact area was successful, as the average adhesion force tested was over double than the adhesion tests without actuation.

7.2 Future Work

This thesis provided the foundation for the design, fabrication, and proof of concept through experimentation of an electroadhesion pad with the use of MFC actuators. The main focus on this research was on obtaining the shear adhesion force. Future work consists of testing the adhesion force in the normal direction to compare with the shear adhesion. Future work involves testing the pad on various other surface materials such as Mylar, Copper, Steel, etc. As shown in Chapter 5, the fabrication method is quite time consuming, so other methods of fabrication are being explored

such as additive material methods. As explained in Chapter 3, it is envisaged to embed strain sensors on the electroadhesion pad in order to create a closed loop environment. As the pad approaches the docking object, the sensors will provide active feedback to the actuator in order to achieve maximum surface adhesion on surfaces with varying curvature.

REFERENCES

- Ashall, F. (1994). *Remarkable discoveries!* Cambridge University Press.
- Brain, W. H., Marshall, & Lamb, R. (2004). "how electricity works" [Computer software manual]. HowStuffWorks.com. Retrieved from <http://science.howstuffworks.com/electricity.htm>
- Busse, T. (2004). Electric field lines [Computer software manual]. APP. Retrieved from <http://whs.wsd.wednet.edu/faculty/busse/mathhomepage/busseclasses/apphysics/studyguides/chapter1516/electricfieldlinespart2.html>
- Clark, N. (2009). An introduction to finite element analysis [Computer software manual]. Engineer's Aspect. Retrieved from <http://anengineersaspect.blogspot.com/2009/06/introduction-to-finite-element-analysis.html>
- Colorado.edu. (2010). Space debris environment [Computer software manual]. Author. Retrieved from http://ccar.colorado.edu/asen5050/projects/projects_2010/borowski/Space_Debris_Environment.html
- Dourmashkin, P. (2004). Visualizing electromagnetism [Computer software manual]. Creative Commons. Retrieved from <http://web.mit.edu/viz/EM/visualizations/coursenotes/modules/guide05.pdf>
- DuPont. (2012). Dupont pyralux lf copper-clad laminates [Computer software manual]. Author. Retrieved from http://www.dupont.com/content/dam/assets/products-and-services/electronic-electrical-materials/assets/PyraluxLFclad_DataSheet.pdf
- Garcia, M. (2013). Space debris and human spacecraft [Computer software manual]. NASA. Retrieved from http://www.nasa.gov/mission_pages/station/news/orbital_debris.html
- Germann, J. (2014). Stretchable electroadhesion for soft robots. *IEEE/RSJ International Conference on Intelligent Robots and Systems*.
- Gokhale, N. (2008). *Practical finite element analysis*. India: Finite to Infinite.
- Inductors and transformers for power electronics.* (2015). Taylor & Francis.
- Kazmeyer, M. (2007). Solid ink vs. laser printers [Computer software manual]. Opposing Views. Retrieved from <http://science.opposingviews.com/solid-ink-vs-laser-printers-1068.html>

- Koh, K. (2014). Experimental investigation of the effect of the driving voltage of an electroadhesion actuator. *Materials*.
- Krape, R. (1968). Applications study of electroadhesive devices [Computer software manual]. NASA. Retrieved from <http://www.worldcat.org/title/applications-study-of-electroadhesive-devices/oclc/755175473>
- Leung, B. (2015). Validation of electroadhesion as a docking method for spacecraft and satellite servicing. *IEEE Aerospace Conference*.
- Liou, J. (2010). An updated assessment of the orbital debris environment in leo. *Orbital Debris Quarterly News*.
- Liu, R. (2012). Wall climbing robot using electrostatic adhesion force generated by flexible interdigital electrodes. *International Journal of Advanced Robotic Systems*.
- Losonc, Z. (2015). Calculation of electrostatic forces in presence of dielectrics [Computer software manual]. energythic. Retrieved from <http://energythic.com/view.php?node=209>
- Monkman, G. (2003). A brief history of electroadhesion [Computer software manual]. Mechatronics.org. Retrieved from <http://www.mechatronics.org/r&d/rob/eag/electroadhesion.pdf>
- Muniraj, C. (2011). Finite element modeling for electric field and voltage distribution along the polluted polymeric insulator. *World Journal of Modelling and Simulation*.
- The oxford companion to the history of modern science*. (2003). Oxford University Press.
- Parness, A. (2013). On-off adhesive grippers for earth-orbit. *AIAA SPACE 2013 Conference and Exposition*.
- Partial differential equations and the finite element method*. (2005). John Wiley & Sons.
- Pelrine, R. (2009). Electroadhesive wall climbing robots and more [Computer software manual]. NASA & SRI International. Retrieved from http://www.nasa.gov/pdf/626527main_3B-5_Pelrine.pdf
- Prazenica, R. J. (2014). Design, characterization, and testing of macro-fiber composite actuators for integration on a fixed-wing uav [Computer software manual]. ERAU.
- Ruffatto, D. (2013). Optimization and experimental validation of electrostatic adhesive geometry. *IEEE Aerospace Conference*.
- Sereda, P. (1965). Electrostatic charging on fabrics at various humidities. *Journ. Textile Inst.*
- Smart-Material. (2015). Smart material - home of the mfc [Computer software manual]. Author. Retrieved from <http://www.smart-material.com/MFC-product-main.html>
- SRI International. (2010). Electroadhesion for industrial, biomedical, military, and consumer applications [Computer software manual]. SRI International. Retrieved from https://www.sri.com/sites/default/files/brochures/sri_electroadhesion.pdf

- The Physics Classroom. (2015). Conductors and insulators [Computer software manual]. Author. Retrieved from <http://www.physicsclassroom.com/class/estatics/Lesson-1/Conductors>
- Tolliver, L., Xu, T.-B., & Jiang, X. (2013). Finite element analysis of the piezoelectric stacked-hybats transducer. Retrieved from <http://stacks.iop.org/0964-1726/22/i=3/a=035015>
- Turner, J. (2007). nasa invention of the year controls noise and vibration [Computer software manual]. NASA Center for Aerospace Information. Retrieved from https://spinoff.nasa.gov/Spinoff2007/ip_9.html
- Udrea, B. (2015). A cooperative multi-satellite mission for controlled active debris removal from low earth orbit. *IEEE Conference*.

A. Mesh Densities for FEA Models

Table A.1 shows the node and element count in the mesh for each assembly analyzed in ANSYS. MESH refinement was used along the regions where highest fidelity was required. A rather dense mesh was created for the insulation layer. Areas between the electrodes were refined even further. A combination of automatic and manual meshing settings were used.

Table A.1. Comparison between multiple gripping methods

Figure	Configuration	Nodes	Elements
A.1	4 Tooth Large Gap	384233	169341
A.2	4 Tooth Small Gap	384387	167924
A.3	Spiral LF9120	1030103	560971
A.4	Spiral LF9130	1038603	569349
A.5	Spiral with Body	1654748	990144
A.6	4 Tooth with Body	616036	215924
A.7	8 Tooth with Body	1050897	653071

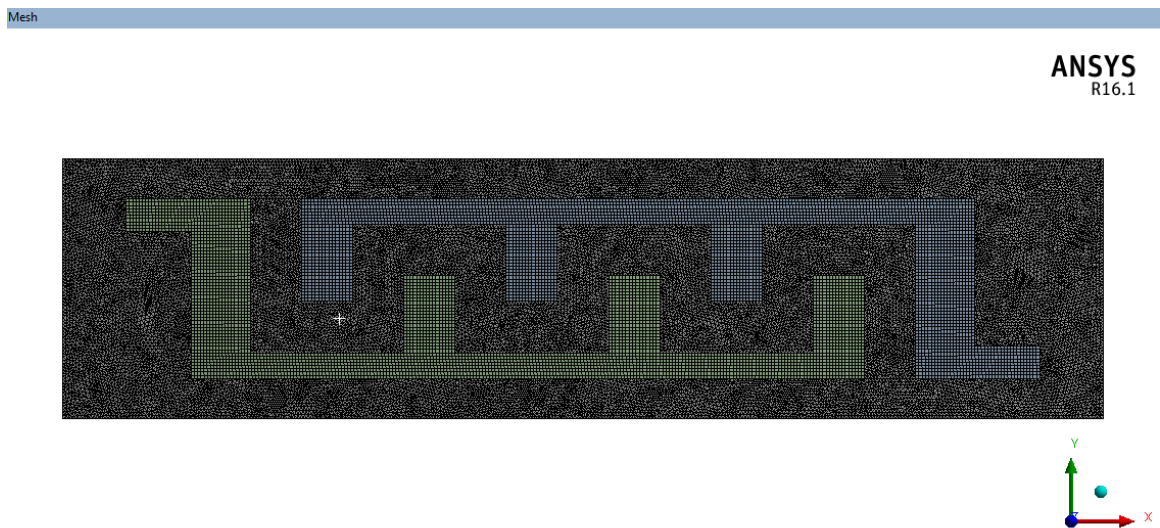


Figure A.1. Mesh Density on Four Tooth - Large Gap Model

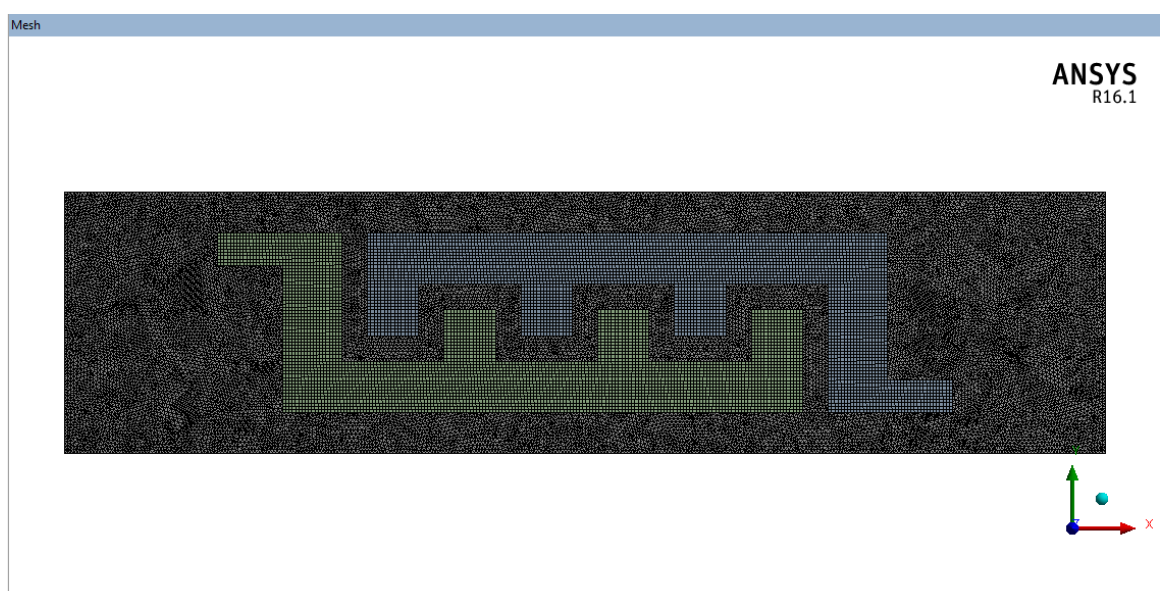


Figure A.2. Mesh Density on Four Tooth - Small Gap Model



Figure A.3. Mesh Density on LF9120 Spiral Model



Figure A.4. Mesh Density on LF9130 Spiral Model



Figure A.5. Mesh Density on Spiral Model with Adhering Body

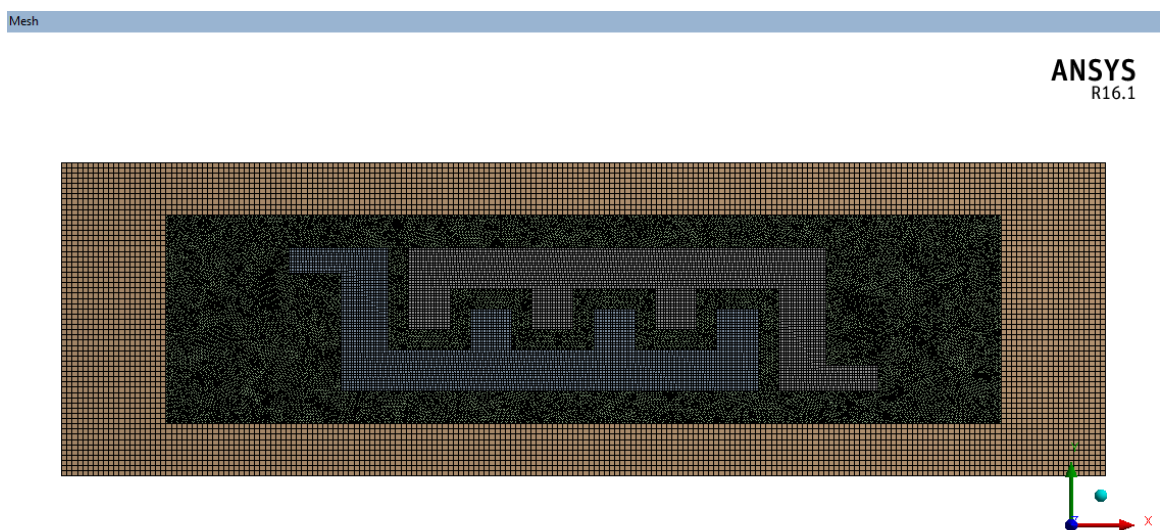


Figure A.6. Mesh Density on Four Tooth Model with Adhering Body



Figure A.7. Mesh Density on Eight Tooth Model with Adhering Body

B. Electroadhesion Pad Adhesion on Curve with MFC

Due to limitations of hardware available at the time of testing, it was rather difficult to test adhesion forces on bodies with large curvature. Figure B.1 shows a hollow cylindrical aluminum body that was used to test the compliance of the electroadhesion pad with the embedded MFC. .

The electroadhesion pad was energized to 3,000 Volts was attempted to attached to the cylindrical body without the use of MFC actuation. Figure B.2 shows how the pad does not adhere very will to the curvature. The pad needed to be placed as close to the surface of the body to gain any adhesion. When the MFC was actuated, the electroadhesion pad conformed to the curvature as shown in Figure B.3. Although no numerical adhesion values was gained out of this test, it is noticeable that the pad is able to latch on to the curvature when the MFC is actuated.



Figure B.1. Hollow Cylinder Used for Curvature Testing



Figure B.2. Electroadhesion Pad with No Actuation



Figure B.3. Electroadhesion Pad With Actuation

C. High Voltage Testing Safety Guidelines

Safety Guidelines for High Voltage Testing

Created by: Walter Saravia

Created for: AE-700 Electroadhesive Pad Design

1. Scope

This document is a written procedure for all testing related to high voltage design of an Electroadhesive pad (AE-700). This document includes safety practices applicable to the ERAU student and ERAU employees who are involved with testing or making measurements on high-voltage or high power sources for this specific project.

2. Definitions

- 2.1 High-Voltage – Any voltage AC or DC potential at or greater than 600 Volts
- 2.2 High-Voltage Testing – shall refer to testing conducted in laboratories where voltages exceed 600 Volts
- 2.3 Qualified Personnel (QP) – Students/Employees who carry out high-voltage testing
- 2.4 Safety Observer – A students or staff who will stand by the outside region of the test area to ensure no one goes inside during testing and to serve as safety contact in case physical harm or potential hazards are seen within the test area during testing
- 2.5 Test Area – The area within the fenced barriers in which high voltage testing will be conducted
- 2.6 AC – Alternating Current
- 2.7 ASTM – American Society for Testing and Materials
- 2.8 OSHA – Occupational Safety and Health Administration

3. Safety Practices – Laboratory Work

3.1 General Requirements

- 3.1.1 All unguarded or ungrounded terminals of the test equipment or apparatus should be considered as energized at all times until verified de-energized by the qualified personnel.
- 3.1.2 Common ground connections must be solidly connected to the test equipment.
- 3.1.3 Precautions must be taken to prevent accidental contact of live terminals by qualified personnel, either by shielding the live terminals or providing physical barriers around the test area. For personnel within the test area, Class 1 insulating gloves shall be worn at all times during testing.
- 3.1.4 High voltage tests will be performed ONLY by personnel who have read and understand this entire document and are knowledgeable in the use of the high voltage power supply.
- 3.1.5 At all times during any testing being conducted, there shall be a safety observer outside the physical barrier.

3.2 Test Areas

- 3.2.1 Permanent test areas are completely enclosed by a physical barrier that is a brightly colored orange fence with the appropriate warning signs such as “DANGER - High Voltage” signs affixed.
- 3.2.2 The test area should never be left unattended while testing is being conducted.
- 3.2.3 No one besides qualified personnel should be allowed within the test area during testing.

3.3 Safety within Test Areas

- 3.3.1 All test equipment will be properly grounded so that hazards to personnel do not exist. The high-voltage circuit from the voltage supply to the specimen setup shall be grounded.
- 3.3.2 All conductors and ground cables used in testing will be rated at a minimum of 6,000V AC. Ratings will be through suppliers that have certified their cables to a certain minimum voltage.
- 3.3.3 Before testing begins, the operator shall wear Class 1 Electrical gloves (which are rated at a minimum of 7,500V AC).
- 3.3.4 QP shall make sure that the test area is completely blocked off and all DANGER - High Voltage signs are visible so that no one else may enter test area.
- 3.3.5 The only device allowed to be used during testing to verify that voltage is present in the system is a Voltmeter.
- 3.3.6 During testing, the QP shall wear no metallic jewelry or any other objects that are electrically conductive.
- 3.3.7 The QP shall wear closed toe shoes and a long sleeved cotton shirt.
- 3.3.8 ONLY the QP shall be inside the barriers during testing.

3.4 Safety Inspection

- 3.4.1 The QP is responsible for inspecting the test area and setup to insure all the safety systems are in place prior to conducting the tests (Refer to section 3.3).
- 3.4.2 Once testing is complete, QP shall unplug power supply and affix the plug within the lockout plug box, and then lock it. The lock key should only be carried by the QP.
- 3.4.3 The filled out tagout attachment shall be placed inside the lock used for the plug lockout box and will be clearly visible. The tag shall only be removed by QP.

4.0 Appendices

Appendix A

Approach Distances for Qualified Personnel

300 V or less	Avoid Contact
300V to 750V	1 ft. 0 in.
750V to 2kV	1 ft. 6 in.
2kV to 15kV	2 ft. 0 in.

Appendix B

Inspection of the Class 1 Rubber Insulating Gloves

- B.1 The gloves shall be visually inspected prior to every set of high voltage tests conducted within the same day per ASTM F496. The visual inspection consists of looking for cuts, holes, tears, embedded objects, and changes in texture).
- B.2 ASTM F496 basically states that each glove shall be filled with air (either manually or with an air pump) and will be checked for leakage. This may consist of listening for escaping air or putting each finger against the cheek to feel for any releasing air.
- B.3 Once testing is complete, the gloves shall be properly stored. Proper storage means that gloves must not be folded and need to be kept out of excessive heat, sunlight, humidity, ozone, and any chemical or substance that could damage the rubber.
- B.4 Per OSHA, dielectric testing for the insulating gloves shall be conducted every 6 months (Reference 1910.137(b)(2)(viii)).

Appendix C

- For any concerns, questions, or comments regarding this guideline or the test setup, please contact:

**WALTER SARAVIA
(703)898-6461
Saravac6@my.erau.edu**

- **For any health or hazardous emergencies that require immediate assistance, please contact:**

**CAMPUS SAFETY
(386)226-6480**

D. Ferric Chloride Etching Safety Guidelines

Safety Guidelines for Ferric Chloride Etching Process

Created by: Walter Saravia

Created for: AE-700 Electroadhesive Pad Design

1. Scope

This document is a written procedure for the ferric chloride etching process, which is used during the manufacturing of electroadhesive pads. The design, manufacturing, and testing of the electroadhesive pads are used for a M.Sc. thesis (AE-700) project. This document includes safety practices applicable to the ERAU student and ERAU employees who are involved with the etching process for this specific project.

2. Definitions

2.1 Ferric chloride – A chemical compound widely used in the process of circuit board etching. Please refer to attached MSDS for specific chemical concentrations.

2.2 Qualified Personnel (QP) – Students/Employees who are involved in the etching process

2.3 Processing Area – The area inside the Machine Shop Lab (LB185) in which the etching process will be conducted

3.1 General Requirements

3.1.1 Before starting the etching process, the QP shall visually inspect the etching tub for any potential leak paths (cracks, holes, etc.) to make sure the ferric chloride will not leak

3.1.2 The QP shall not wear any jewelry that may come in contact with the ferric chloride, such as watches, necklaces, bracelets, etc. in the event of the solution splashing

3.1.3 In order to prevent any eye injuries due to accidental spills or splashes, the QP performing the etching shall wear safety goggles with lateral protection at all times during the etching process from the time it is poured into the tub until the moment the unused solution is bottled back up for disposal

3.1.4 The QP shall wear rubber gloves (latex or nitrile) before pouring the ferric chloride, during the etching process, and up until it is properly stored back in a container for proper disposal

3.2 Processing Areas

3.2.1 Any copper etching related to this project shall be done in LB185 ONLY, due to the proper ventilation fans present in the room

3.2.2 The area where the etching process is occurring should never be left unattended while the ferric chloride is still in the tub

3.2.2 The area where the etching process is occurring should be relatively clean and far away from any equipment that might be negatively affected in the event that splashing occurs

3.3 Solution Disposal

3.3.1 A bucket with tap water shall be used in order to rinse off the excess solution on the pads once etching has been completed

3.3.2 pH strips shall be used to test the levels of the mixed solution in the bucket. The solution pH must range between 2 and 12.5 in order to be allowed to be poured onto the drains. Otherwise, store the solution for proper hazardous waste disposal (contact Bill Russo)

3.4 Solution Storage

3.4.1 The ferric chloride shall be stored in a locked “hazardous chemical” cabinet located in LB185

3.4.2 The ferric chloride shall be stored in a corrosive resistant plastic container (such as the container it was originally sent in). The container shall be kept in a dry and clean area, away from incompatible substances (corrosive substances)